Journal of Materials Chemistry C

ROYAL SOCIETY OF CHEMISTRY

REVIEW

View Article Online
View Journal | View Issue

Cite this: J. Mater. Chem. C, 2024, 12, 12218

Lanthanide-based nanothermometers for bioapplications: excitation and temperature sensing in optical transparency windows

Natalia Jurga, Marcin Runowski and Tomasz Grzyb *

Nanoparticles containing lanthanide (Ln^{3+}) ions in their structure have become one of the most important tools in nanomedicine, mainly due to their appealing spectroscopic properties. The unique energy level structure of Ln^{3+} allows for the generation of characteristic luminescence, which depends highly on the temperature. It is possible to use the intensity ratio between two emission lines of a single Ln^{3+} ion or the emission of two different ions to monitor the system's temperature. This approach often leads to the high sensitivity of such thermometers; however, the most important is the possibility of remote temperature sensing. That property allows for monitoring various physiological processes in living organisms and is helpful in theranostics. What is essential for bioapplications is that the excitation and emission wavelengths of Ln^{3+} ions can occur within three spectral ranges, known as optical transparency windows (biological windows). The biological materials, such as tissues, are transparent to radiation with wavelengths in the ranges of 750–950 nm, 1000–1350 nm and 1500–1800 nm. In this article, we review the state of the art regarding nanoparticles doped with Ln^{3+} ions for applications in temperature sensing within optical transparency windows regarding both excitation and emission wavelengths. The information provided in our review article will enable the selection of the type of nanothermometer for specific applications, help in selection of the emission or excitation wavelength, understanding the differences between systems based on down-shifting and upconversion phenomena, recognizing differences in the thermosensitive properties of various lanthanide ions, such as Nd^{3+}, Tm^{3+}, or Er^{3+}, as well as the matrices and chemical compounds that form the basis for nanoparticles.

Received 20th December 2023,
Accepted 12th July 2024

DOI: 10.1039/d3tc04716d

rsc.li/materials-c

1. Introduction

Temperature is considered one of the most fundamental state functions and the most frequently used and investigated thermodynamic parameter.[1,2] Increased temperature may accelerate most chemical reactions, as well as biological and physical processes occurring in nature and laboratory conditions. That is why its precise and accurate monitoring is highly important in various industrial, scientific, environmental, and biological processes.[3–5] The latter area is also strictly related to modern biomedicine, where continuous and online temperature regulation is utilized in medical diagnosis, disease treatment and general healthcare purposes.[6–8]

Temperature detection has been realized in diverse manners for centuries. Nowadays, the most commonly used thermometers are based on (I) liquid solvents or mercury, utilizing their thermal expansion properties for temperature detection; (II) the thermoelectric effect used in thermocouples; (III) resistance thermometers, which measure the temperature-dependent electrical resistivity; and (IV) pyrometers, which optically detect the body's infrared radiation by correlating it with the temperature of the analysed object.[1,2,9] Nevertheless, in all cases (except the latter one), a mechanical or electrical connection with the measuring object must be maintained, significantly hampering remote and non-invasive temperature detection, *e.g.* inside the human body, in a closed mechanical system or the small-sized, *i.e.* micro- and even nanosized areas.[1,2,9,10] Although pyrometers do not need any solid connection with a measured object, they provide temperature readouts only from the body's surface; they have low accuracy and spatial resolution, typically allowing rough temperature estimations of bulk, macroscale objects.[1–3]

The mentioned issues can be easily addressed and solved by the luminescence (nano)thermometry technique, which is based on noninvasive, remote detection of temperature based on monitoring the temperature-induced changes of some luminescence features of optically active probes (luminescent materials), allowing temperature monitoring in microscopic and nano-sized areas.[10–15] In other words, this technique utilizes temperature-dependent steady-state or time-resolved spectroscopic features for remote temperature sensing, such as luminescence/fluorescence intensity ratio (LIR/FIR), signal intensity, spectral position of the emission line, full-

Department of Rare Earths, Faculty of Chemistry, Adam Mickiewicz University, Poznań, Uniwersytetu Poznańskiego 8, 61-614 Poznań, Poland.
E-mail: tgrzyb@amu.edu.pl

width-at-half maximum (FWHM) of the band, or luminescence decay/rise times, respectively.[9–13,16–19] Each of these factors can be used as a "thermometric parameter", whose change can be correlated and calibrated with temperature of the system.[10,16,17] The most frequently used thermometric parameters are LIR/FIR and emission decay time. The first one can be monitored in a facile way using standard detection systems, but it can also be easily biased by the reabsorption/scattering effects and by variations of the on-target excitation power density when performing the measures in a real system, *e.g. in vitro* or *in vivo* experiments.[10,20,21] On the other hand, the second approach is not biased by the mentioned factors and can provide accurate temperature readouts in different environments. However, the time-resolved experiments are generally much more complicated, requiring pulse excitation sources and fast detection systems.[10] Nowadays, researchers try to combine both approaches, *i.e.* different sensing strategies in multi-modal and multi-parameter temperature detection, which benefits from improved sensing reliability.[10,22–24]

Luminescent thermometers, *i.e.* optical temperature probes, are typically made of inorganic luminescent materials based on lanthanide (Ln^{3+}) ions, d-block metal ions, quantum dots or other optically active nanoparticles (NPs).[9,19,22,24] Among them, Ln^{3+}-doped materials play a leading role, mainly due to their unique optical properties, including luminescence covering a broad spectral range from UV to visible and NIR, presence of narrow absorption and emission lines, rich ladder-like energy levels structure, long luminescence decay times (μs–ms), and so forth.[9,25–29] Moreover, Ln^{3+}-doped inorganic materials and NPs may exhibit not only classical down-shifting emission upon UV-visible excitation (Stokes-type process) but also upconversion (UC) emission (anti-Stokes) upon a low-energy near-infrared (NIR) laser excitation.[25,30–34] The UC process is a non-linear and non-parametric process, where absorption of two or multiple photons leads to generating one higher energy photon.[35] In such case, it is possible to use the low-energy NIR laser radiation coinciding with the 1st, 2nd or 3rd biological window (BW) and produce emissions in the 1st or 2nd BW, which is highly beneficial from the point of view of various biomedical applications. Nevertheless, one of the most beneficial features of Ln^{3+} ions for temperature sensing is the presence of thermally-coupled levels (TCLs) in most Ln^{3+} ions, *i.e.* mainly excited states typically separated by 200–2000 cm^{-1}.[9,11] Such energy separation (ΔE) ensures decent population of both TCLs within a typically utilized T-ranges, including cryogenic, room temperature and high-T ranges.[10,12] This feature is utilized for LIR-based optical thermometers, allowing ratiometric temperature detection, which is much more reliable than sensing based on the intensity of a single band. The most commonly used Ln^{3+} activator ions for temperature sensing are Er^{3+} ($\Delta E \approx$ 700–850 cm^{-1}), Tm^{3+} ($\Delta E \approx$ 1500–2000 cm^{-1}), Nd^{3+} ($\Delta E \approx$ 1000–1100 cm^{-1}) and Pr^{3+} ($\Delta E \approx$ 500–600 cm^{-1}).[9–12]

On the other hand, the most frequently chosen materials to host the selected Ln^{3+} ions are inorganic fluorides, simple and mixed/complex oxides, phosphates, vanadates, silicates, borates, tungstates, molybdates, among which the most commonly used compound is $NaYF_4$:Yb^{3+},Er^{3+} (as NPs), which has low phonon energy and provides bright UC luminescence.[26,28–31] Utilization of the mentioned inorganic nanomaterials is associated with several factors, such as their high-temperature stability, low-phonon energies allowing the generation of UC emission, insolubility in water, as well as facile synthesis in the form of NPs.[25,26,36–38] The latter feature is crucial for the development of Ln^{3+}-based luminescent nanothermometers, *i.e.* nano-sized optical probes of temperature, which allow temperature detection with excellent spatial resolution, which is important in thermal sensing and imaging of microscopic and nanoscopic objects.[11,16,20,39–41] Using luminescent nanothermometers enables remote and non-invasive temperature monitoring in living organisms by introducing optically active NPs into the body fluids, tissues and single cells.[16,40,41] Generally, using the nanothermometry approach is desirable in all situations where classical macroscopic thermometers are impossible, impractical, or inconvenient, *i.e.*, in such applications, where the sensor size plays a vital role.[42–44]

One of the most extensively studied sub-fields in optical sensing is temperature detection in biological systems, *i.e.* remote monitoring of temperature gradient in cells/tissues and in the whole human or animal body, performed inside a living organism (*in vivo*) or outside it in laboratory experiments (*in vitro* and *ex vivo*).[4,6,7] Such studies are performed to examine temperature distribution in a given tissue, monitor temperature elevation due to some disease-related problems (*e.g.* tumour growth), analysis of optical heating processes during laser-induced cell damage, photodynamic therapy, hyperthermia, controlled drug release therapies, and so forth.[4–7] The selection of appropriate luminescent nanothermometers for diverse bioapplications should depend on their spectral characteristics, *i.e.*, the possibility of photo-excitation and the presence of emission lines in the biological transparency windows, where the light absorption and scattering effects by water, tissues and blood are minimal. In general, we can distinguish three spectral ranges, called 1st BW (≈750–950 nm), 2nd BW (≈1000–1350 nm) and 3rd BW (≈1500–1800 nm), where the mentioned effects are minimized (see Fig. 1).[40,45–47] All of them are located in the low-energy NIR spectral ranges, which is beneficial for bioapplications, in contrast to excitation and detection in the UV and visible ranges. This is because the high-energy excitation light sources generating light in the UV and visible ranges (especially lasers) may easily damage the irradiated tissues and transform healthy cells into tumour ones. Moreover, in the case of temperature sensing in biological systems, the excitation and detection outside the BWs range frequently lead to significantly biased temperature readouts because of the discussed reabsorption and scattering effects of the surrounding media, as well as due to the enhanced optical heating upon laser irradiation.[20]

The most frequently used equation in luminescence thermometry is associated with the Boltzmann-type distribution of the electrons in a thermal equilibrium, which typically occupies excited states separated with a relatively small ΔE value. This equation fits the determined LIR values and correlates them with temperature. It is commonly expressed in the following form ref. 9:

$$\mathrm{LIR} \equiv \frac{I_2}{I_1} = B\exp\left(-\frac{\Delta E}{k_B T}\right) \quad (1)$$

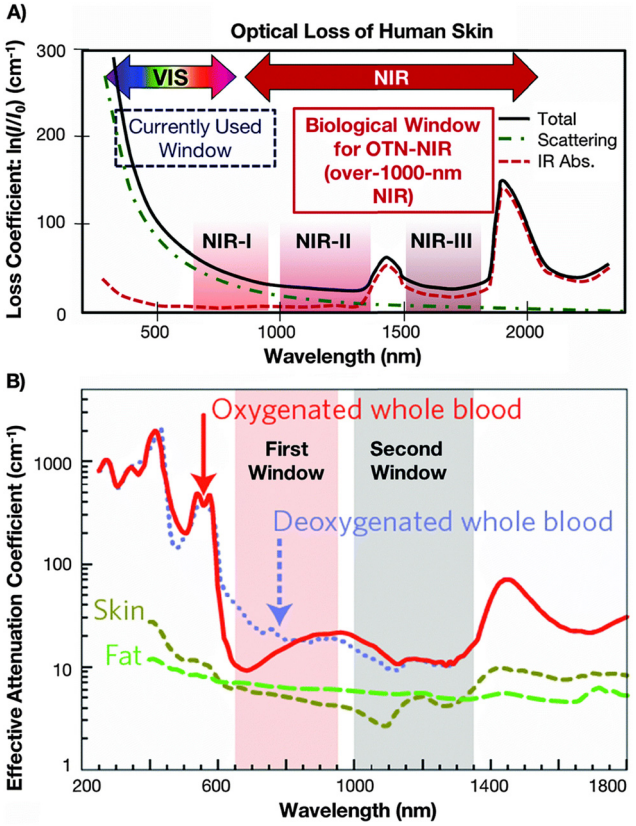

Fig. 1 (A) Absorption spectrum of human skin showing the 1st, 2nd and 3rd biological windows. (B) Zoom in on the two first optical windows in some biological tissues and fluids. These plots of effective attenuation coefficient (on a logarithmic scale) *vs.* wavelength show the quantitative relevance of different body substances (oxygenated blood, deoxygenated blood, skin and fatty tissue) when aiming for deep sub-skin imaging. Used with permission of The Royal Society of Chemistry from ref. 47; permission conveyed through Copyright Clearance Center, Inc.

where LIR is the luminescence intensity ratio of two thermalized emission bands associated with emissions from the given TCLs of Ln^{3+} ions; I_2 is the intensity of the higher-energy band, and I_1 corresponds to the intensity of the lower-energy band; ΔE is the energy separation between two TCLs, which is typically obtained from fitting of the experimental data to eqn 1, or it is derived from the emission spectra by calculating the differences in energies of two thermalized bands; T is the absolute temperature; k_B is the Boltzmann constant; and B is a constant which depends on degeneracies of states, transitions angular frequencies, rates of total spontaneous emission, as well as branching ratio of the transitions in respect to the ground state.[9,48] It is worth noting that the thermal relations of non-TCLs are often used for optical temperature sensing, where the dependences of LIR of the non-thermalized bands are used.[16,49] In this situation, the observed changes in the relative band intensities, so in the LIR values, may originate from temperature-dependent energy transfer (ET) and quenching processes, which vary for different radiative transitions.[10,12] In such cases, the determined LIR values are correlated with temperature by fitting to some empirical functions (the phenomenological models are used in the case of absence of a proper physical model conforming to the observed changes), *e.g.* higher-order polynomials or exponential functions.[10,16,50] Similarly, it is possible to fit and correlate the luminescence decay times, FWHM of the emission band, signal intensity, or other selected thermometric parameters with temperature. Using the kinetics of the excited state as a thermometric parameter offers an extra benefit, *i.e.* unlike the ratiometric method, the lifetime of the excited state remains unaffected by light absorption or scattering as it travels through the medium between the thermometric phosphor and the detector. Consequently, in this scenario, the reliability of luminescent thermometers based on lifetime is anticipated to be higher.[44]

To quantitatively evaluate the sensing performance of any luminescent thermometer, the absolute (S_a) and relative (S_r) temperature sensitivities are commonly determined using the following equations:[9]

$$S_a = \frac{dSP}{dT} \quad (2)$$

$$S_r = 100\% \times \frac{1}{SP}\frac{dSP}{dT} \quad (3)$$

where SP is the spectroscopic parameter analysed. However, for comparisons of different LIR-based optical thermometers between different laboratories, optical setups, and thermometric parameters, only the S_r value is a valid and reliable figure of merit, as it does not depend on the mentioned factors (apparatus effects). The S_r informs how the selected thermometric parameter changes per 1 °C of the absolute temperature. Another important parameter is temperature resolution (δT), *i.e.*, uncertainty of sensing. It takes into account the uncertainty of determination of the measured spectroscopic parameter (δSP), which is associated with signal-to-noise ratio, and it can be theoretically estimated *via* the following general formula:[9]

$$\delta T = \frac{1}{S_r}\frac{\delta SP}{SP} \quad (4)$$

In developing new luminescent thermometers, one should also consider factors such as the signal intensity of the phosphor used (which depends on its quantum yield and brightness), which typically decreases with temperature, and the thermal stability of the sensor used.[10,12] The latter can be determined by performing the thermal cycling experiments, *i.e.* by monitoring how the selected luminescence features change during several cycles of material heating and cooling between two extreme temperature values to confirm the sensing repeatability.[12] Obviously, the selected SP should not change after the thermal cycling experiments, *i.e.* it should be constant at fixed temperature values, and any deviations may indicate the thermal instability/decomposition of the material studied.

As there are thousands of reports dealing with luminescence thermometry,[10] in this review article, we focus only on lanthanide-based luminescent thermometers, operating strictly within the 1st, 2nd or 3rd BW. Here, we assume this requirement is fulfilled only if excitation and emission wavelengths originating from Ln^{3+} ions are within the BWs' spectral ranges. Hence, we do not discuss the numerous reports showing the use of

975/980 nm excitations, even if the emission of the corresponding thermometer is located in the NIR range of any BW. This is because, in the abovementioned cases, the change (deterioration) in excitation flux caused by significant absorption and light scattering by the body fluids around 975 nm (outside the 1st and 2nd BW) alters the on-target laser power density.[20,51] This often underestimated effect may bias the majority of temperature readouts, especially in the case of upconverting materials and thermometers utilizing non-TCLs.[10,20,52] Moreover, using a 975 nm laser for excitation often causes undesired optical heating effects and artificial elevation of the local temperature of the sample, which is usually much stronger than, *e.g.* by using ≈808 nm or 1532 nm excitations.[53] The selection of the excitation wavelength of NPs in a medium containing water is of great significance for the resulting luminescence and potential optical heating of water. The absorption properties of the biological system components are the most important issue that may lead to the reabsorption of radiation from NPs.[54] However, water itself can absorb excitation radiation, causing heating. It has been demonstrated that using excitation outside the BWs, such as 980 nm, results in significant water heating, which was not observed with an 808 nm wavelength.[55] The authors showed, that the use of a 980 nm laser with a power density of 140 W cm^{-2} causes water to heat up by 3.5 °C after 25 minutes of irradiation. In contrast, an 808 nm laser with the same power heats the water under the same conditions by approximately 1 °C. The presence of NPs absorbing the excitation radiation additionally increases this effect by about 0.5 °C.[55]

The properties of NPs in temperature detection are most commonly studied in the form of colloids or powders. Some publications have also demonstrated simple *ex vivo* experiments verifying the utility of nanothermometers in real biological systems.[8,41,56–60] However, this does not change the fact that nanothermometry using the emission of Ln^{3+} ions requires much more work and research to ultimately verify whether practical utilization of Ln^{3+}-doped NPs in temperature detection is valid and reliable. A compelling example prompting a reconsideration of strategies and enriching thermometry research with *in vivo* studies is the work published by Shen *et al.*,[61] which presents specific examples of how different types of NPs behave in biological systems studied *in vivo*. Scientists have shown that distortions in the emission spectra resulting from skin tissue absorption are evident. Indeed, they affect the intensity ratio between emissions at 980 and 1060 nm, which, in turn, is commonly used for thermal sensing, for example, in systems involving Yb^{3+}, Er^{3+}, or primarily Nd^{3+} ions.[62–65] The absorption by the skin additionally diminishes the emission bands around 1230 and 1470 nm of Tm^{3+}, which is also employed for ratiometric thermal sensing.[66]

2. Down-shifting nanothermometers

Ln^{3+} ions exhibit excellent NIR down-shifting emission with long excited state lifetimes, large tissue penetration depths, good efficiency, and photochemical stability. Nanothermometers based on down-shfted luminescence are listed in Table 1. One of the best ions for nanothermometry based on down-shifted luminescence is Nd^{3+}. Because of the spectral overlap of the emission bands with the transparency windows of human tissues, NPs doped with Nd^{3+} ions emerge as relevant sub-tissue optical probes. Most commonly in the literature, an excitation wavelength of 808 nm and an intensity ratio between Stark levels (crystal-field components) within 880–1060 nm range is employed. However, Nd^{3+} ions may also emit longer wavelength NIR light, *i.e.* around 1320 nm (see Fig. 2). Unlike in UCNPs, the excitation and emission fall into the highest transparency window of tissues within the NIR spectral region. Moreover, the Stokes emission quantum yield (QY) is at least one order of magnitude higher than the QY of upconversion, which makes Nd^{3+}-doped NPs the most promising for bioapplications. Nd^{3+}-doped NPs allow temperature sensing and bioimaging in the NIR range by simultaneous excitation within the 1st BW, *i.e.*, at around 808 nm. Examples of such applications are experimental studies reported by Savchuk *et al.*,[67] Quintanilla *et al.*[68] or Cantarano *et al.*[69] The studies of Nd^{3+}-based nanothermometry are the most frequent, and much information can be drawn from the below-discussed ones. Nd^{3+}-based nanothermometer performance is highly dependent on Nd^{3+} concentration, which Maciejewska *et al.*[70] demonstrated. According to these results, Nd^{3+} concentration also determines the range in which the thermometer can be applied. Moreover, it seems crucial to select appropriate Nd^{3+} emission lines for the high sensitivity of the thermometer. Examples of works presenting different LIRs taken from Nd^{3+}-doped NPs are those published by Gschwend *et al.*,[71] Skripka *et al.*[59] or by Debasu *et al.*[72] Below, we discuss four groups of down-shifted nanothermometers: (i) based on Nd^{3+}-only-doped NPs, (ii) systems in which Nd^{3+} played a role of sensitizers and another Ln^{3+} ions, together with Nd^{3+} were emitters (*e.g.* $NaGdF_4$:Yb^{3+},Tm^{3+}@$NaYF_4$:Yb^{3+}@$NaGdF_4$:Yb^{3+}, Nd^{3+}@$NaGdF_4$),[73] (iii) NPs in which Tm^{3+} ions were used as sensitizers for luminescence (*e.g.* $KLu(WO_4)_2$:Ho^{3+},Tm^{3+})[74] and (iv) NPs doped with Yb^{3+} ions as sensitizers (*e.g.* CaF_2:Yb^{3+}/Er^{3+}/Tm^{3+}).[75]

2.1. Nanoparticles doped with Nd^{3+} ions only, excitable within the 750–808 nm range

Nd^{3+} ions seem to be excellent lanthanide dopants for observing luminescence signals in the range of biological windows. Nd^{3+} ions are capable of bright emission at around 880 and 1060 nm, corresponding to the $^4F_{3/2} \rightarrow {}^4I_{9/2}$ and $^4F_{3/2} \rightarrow {}^4I_{11/2}$ transitions, respectively. Usually, the emission band connected with $^4F_{3/2} \rightarrow {}^4I_{9/2}$ transition is composed of several sub-bands related to the Stark energy sublevels of both $^4F_{3/2}$ and $^4I_{9/2}$ manifold state (Fig. 3). The ratio between sub-bands at around 860 and 870 nm shows temperature dependence. One of the first reports on the thermal behaviour of these bands was published by Wawrzynczyk *et al.*,[79] who studied $NaYF_4$:Nd^{3+} cubic NPs under excitation at 830 nm. The analysis of Stark components of $^4F_{3/2} \rightarrow {}^4I_{9/2}$ transition bands indicated the dependence of LIR on temperature and shift of the bands' maxima. The researchers calculated the relative sensitivity of the studied NPs, which was 0.12% $°C^{-1}$ at 0 °C.[79]

Rocha *et al.*[65] demonstrated the thermal behaviour of Nd^{3+}-doped LaF_3 core@shell NPs under excitation with an 808 nm

Table 1 Nanothermometers based on down-shifted luminescence

Type of nanoparticles	Emmiter	λ_{ex} (nm)	Emission bands used (nm)	Reported max. sensitivity	Reported T-range (°C)	Sensing parameter	Comments	Bioapplications in real conditions	Ref
$Bi_2SiO_5:Nd^{3+}$	Nd^{3+}	808	LIR = 867/898	S = 0.34% °C^{-1} at 37 °C	20–65	LIR			76
$Y_3Ga_5O_{12}:Nd^{3+}$	Nd^{3+}	808	LIR = (870–873.5)/(879.75–886.7)	S = 0.13% °C^{-1} at 77 °C	22–77	LIR			77
$LaF_3:Nd^{3+}$	Nd^{3+}	808	LIR_1 = 861/863; LIR_2 = 885/865	S_1 = 0.4% °C^{-1}; S_2 = 0.2% °C^{-1}; ΔT = 0.7 °C	20–60	LIR	Researchers presented how annealing improves the sensitivity of nanothermometers.	*Ex vivo* sub-tissue time-resolved thermal sensing experiments.	78
$LiNdP_4O_{12}$	Nd^{3+}	808	LIR = 866/870	S = 0.22% °C^{-1} at 40 °C; ΔT = 1.13 °C	32–83	LIR		*Ex vivo* experiments with chicken breast as a biological tissue phantom for investigation of the penetration depth of both excitation and emission light.	57
$NaYF_4:Nd^{3+}$	Nd^{3+}	830	LIR = 863/870	S = 0.12% °C^{-1} at 0 °C	0–150	LIR			79
$NaNdF_4@NaYF_4@NaYF_4:Nd^{3+}$	Nd^{3+}	808	LIR = 857/863	S = 0.11% °C^{-1}	−196 to 277	LIR	The researchers investigated the influence of power density on temperature readout.		80
$LaF_3:Nd^{3+}$ + Fe_3O_4 polymer nanocapsules	Nd^{3+}	808	LIR = 862.5/864	S = 0.4% °C^{-1}	25–60	LIR	Two types of NPs – luminescent and magnetic were encapsulated in polymer nanospheres.	*Ex vivo* experiments using lamb's heart for photo-induced heating and temperature reading.	8
$LiLuF_4:Nd^{3+}$	Nd^{3+}	808	LIR = 862/866	0.62% °C^{-1} at −196 °C	−196 to 2	LIR	Nanothermometry for low-temperature ranges.		81
$Y_3Al_5O_{12}:Nd^{3+}$	Nd^{3+}	760	LIR = 880/946	S = 0.13% °C^{-1} at 30 °C; ΔT = 9.7 °C	30–120	LIR	Report an automated machine learning tool that retrieves an optimal pipeline to enhance the response of thermometers.		82
$LaF_3:Nd^{3+}$	Nd^{3+}	808	LIR = 865/885	S = 0.26% °C^{-1}	32–72	LIR		NPs acted simultaneously as nanoheaters and temperature sensors studied *in vivo*.	83
$ALaP_4O_{12}:Nd^{3+}$ (A = Li, K, Na, Rb)	Nd^{3+}	808	LIR = 865/870	S = 0.47% °C^{-1} (band position); S = 0.46% °C^{-1} (FWHM); S = 0.31% °C^{-1} (LIR)	−190 to 327	LIR, band position, FWHM	Three temperature-dependent parameters as functions of Nd^{3+} dopant concentration were investigated.		84
$Y_3Al_5O_{12}:Nd^{3+}$	Nd^{3+}	793	LIR = 941/949	S = 0.20% °C^{-1}	20–40	LIR		The obtained NPs were used for NIR bioimaging	69
$Y_3Al_5O_{12}:Nd^{3+}$	Nd^{3+}	808	LIR = 938/945	S = 0.15% °C^{-1}	10–70	LIR		The application of NPs for submicrometric thermal sensing and imaging of different systems.	85
$Gd_3Sc_2Al_3O_{12}:Nd^{3+}$	Nd^{3+}	806	LIR = 946/936	S = 0.21% °C^{-1} at 20 °C	20–50	LIR			86
$YVO_4:Nd^{3+}$	Nd^{3+}	808	LIR = 1063.9/1065.3	S_1 = 0.54% °C^{-1} (LIR); S_2 = 0.75% °C^{-1} (band position) both at 30 °C	−150 to 25	LIR, band position			64
$CaF_2:Nd^{3+},Y^{3+}$	Nd^{3+}	808	LIR = 1053/1062	S = 0.18% °C^{-1} at 22 °C	22–62	LIR		The penetration depth of NPs was investigated *ex vivo* using chicken breast.	58

Table 1 (*continued*)

Type of nanoparticles	Emmiter	λ_{ex} (nm)	Emission bands used (nm)	Reported max. sensitivity	Reported *T*-range (°C)	Sensing parameter	Comments	Bioapplications in real conditions	Ref
CaF_2:Nd^{3+},Y^{3+}	Nd^{3+}	808	LIR = (1014–1057)/(1057–1074 nm)	n/a	37–100	LIR		Tracking temperature in 3D tumour spheroids.	68
TiO_2:Nd^{3+}	Nd^{3+}	808	LIR = 1060/1340	S = 0.86% °C^{-1} at 27 °C; ΔT = 1.1 °C	27–70	LIR	The effect of the annealing temperature of NPs on the thermal sensitivity was studied.		87
BaB_2O_4:Nd^{3+} and BaB_2O_4:Yb^{3+},Nd^{3+}	Nd^{3+}	804	LIR_1 = 1060.5/1067.5; LIR_2 = 1050.0/1058.5	S_1 = 0.23% °C^{-1}; S_2 = 0.06% °C^{-1}	25–55	LIR			88
LaOCl:Nd^{3+} and LaOCl:Nd^{3+}@LaOCl	Nd^{3+}	808	LIR = 1066/1090	S = 0.26% °C^{-1} at 27 °C	5–60	LIR	Different concentrations of Nd^{3+} ions do not affect the relative sensitivity.		89
LaF_3:Nd^{3+}@LaF_3	Nd^{3+}	808	LIR = 900/1060	S = 0.13% °C^{-1}; ΔT = 1.2 °C	10–60	LIR		The authors tested sub-tissue penetration length under 808 nm excitation using phantom tissues. NPs were tested as reference nanothermometers in single-beam subtissue hyperthermia treatments.	65
Gd_2O_3:Nd^{3+}	Nd^{3+}	808	LIR between Stark levels within 1250–1550 range	S = 0.23% °C^{-1} at 30 °C	30–120	LIR			90
YVO_4:Nd^{3+}	Nd^{3+}	808	LIR_1 = 879/887; LIR_2 = 1063/1072	S_1 = 0.19% °C^{-1}; S_2 = 0.15% °C^{-1}	25–60	LIR		*Ex vivo* experiments were presented to determine the penetration depth.	56
$KGd(WO_4)_2$:Nd^{3+}	Nd^{3+}	808	LIR_1 = 895.8/883.8; LIR_2 = 1075.8/1067.6	S_1 = 0.12% °C^{-1}; S_2 = 0.16% °C^{-1}	35–60	LIR		NIR imaging in biological tissue with use of Nd^{3+}-doped NPs	67
$BiVO_4$:Nd^{3+}	Nd^{3+}	750	LIR_1 = (872–877)/(902–907); LIR_2 = (1059–1066)/(1066–1071); LIR_3 = (790–840)/(840–945); LIR_4 = (790–840)/(1030–1130)	S_1, S_2 < 0.14% °C^{-1}; S_3 = 1.47% °C^{-1}; S_4 = 1.53% °C^{-1} at 37 °C	25–302	LIR	The authors compared how the selection of emission bands influences received sensitivities.	*Ex vivo* experiments show nanothermometers' potential for deep-tissue thermal sensing in real-time with chicken skeletal muscle tissue.	71
$LiLuF_4$:Nd^{3+}@$LiLuF_4$	Nd^{3+}	793	LIR_1 = (866.2–869.6)/(883.2–884.2); LIR_2 = (866.2–869.6)/(912.5–913.7); LIR_3 = (1045.3–1049)/(1055.9–1057.2); LIR_4 = (1050.7–1055.9)/(1055.9–1057.2); LIR_5 = (1316.7–1328.3)/(1328.4–1329.7)	S_1, S_2 = 0.58% °C^{-1}; S_3, S_4 = 0.48% °C^{-1}; S_5 = 0.49% °C^{-1} at 20 °C	20–45	LIR	The researchers compared all of the Nd^{3+} bands for the best sensitivity.	*Ex vivo* experiments with the use of pork fat for determination of heating-cooling dynamics and applicability of NPs as *in situ* thermometers.	59

Table 1 (*continued*)

Type of nanoparticles	Emmiter	λ_{ex} (nm)	Emission bands used (nm)	Reported max. sensitivity	Reported *T*-range (°C)	Sensing parameter	Comments	Bioapplications in real conditions	Ref
Gd_2O_3:Nd^{3+}	Nd^{3+}	808	LIR_1 = 927/942; LIR_2 = 1055/1076; LIR_3 = 1320/1353	S_1 = 2.18% °C^{-1}; S_2 = 0.3% °C^{-1}; S_3 = 0.61% °C^{-1}; at 25 °C; ΔT = 1.2 °C	25–65	LIR	The researchers compared three ranges of Nd^{3+} emission for the best sensitivity.		72
Y_2O_3:Nd^{3+}	Nd^{3+}	808	LIR_1 = 898/914; LIR_2 = 877/893; LIR_3 = 1053/1075; LIR_4 = 1057/1080	S_1 = 0.23% °C^{-1}; S_2 = 0.31% °C^{-1}; S_3 = 0.43% °C^{-1}; S_4 = 0.37% °C^{-1}	25–60	LIR	The authors compared the relative sensitivities calculated using various Stark components of Nd^{3+} transitions.		91
$LaPO_4$:Nd^{3+},Er^{3+}	Nd^{3+}, Er^{3+}	808	LIR = 1300/1540	S_1 = 1.15% °C^{-1} (LIR); S_2 = 2.3% °C^{-1} (lifetimes) at 327 °C	−196 to 327	LIR and lifetimes			92
Y_2O_3:Er^{3+},Nd^{3+}	Nd^{3+}, Er^{3+}	808	LIR_1 = 935/943; LIR_2 = 1084/1100; LIR_3 = 1559/1551	S_1 = 0.45% °C^{-1}; S_2 = 0.43% °C^{-1}; S_3 = 0.17% °C^{-1} at 25 °C	25–400	LIR			93
$NaGdF_4$:Yb^{3+},Tm^{3+}@$NaYF_4$:Yb^{3+}@$NaGdF_4$:Yb^{3+}, Nd^{3+}@$NaGdF_4$	Nd^{3+}, Tm^{3+}	808	LIR_1 = 1330/1215; LIR_2 = 1470/1215	S_1 = 0.92% °C^{-1}; S_2 = 1.07% °C^{-1} at 30 °C	10–90	LIR	ET and CR processes were responsible for the intense emission of Tm^{3+} and Nd^{3+} ions.	Temperature detection and NIR bioimaging were demonstrated *in vivo.*	73
$NaGdF_4$:Er^{3+},Ho^{3+},Yb^{3+}@ $NaGdF_4$:Yb^{3+}@$NaGdF_4$:Nd^{3+},Yb^{3+}	Nd^{3+}, Er^{3+}, Ho^{3+}	806	LIR_1 = 1180/1340; LIR_2 = 1550/1340	S_1 = 1.1% °C^{-1}; S_2 = 1.15% °C^{-1} at 20 °C; ΔT = 0.8 and 1.2 °C	20–50	LIR	Multishelled NPs allowed for LIR calculation within 2^{nd} (Ho^{3+}/Nd^{3+}) and 3^{rd} (Er^{3+}/Nd^{3+}) BWs.		55
$NaYF_4$:Yb^{3+},Ho^{3+}@$NaYF_4$:Yb^{3+}, Er^{3+}@$NaNdF_4$:Yb^{3+} and $NaYF_4$:Yb^{3+},Er^{3+}@$NaYF_4$:Yb^{3+}, Ho^{3+}@$NaNdF_4$:Yb^{3+}	Er^{3+},Ho^{3}	808	LIR = 1164/1534	S = 0.88% °C^{-1} (Ho@Er); S = 1.30% °C^{-1} (Er@Ho) at 55 °C	25–55	LIR		An *ex vivo* experiment was conducted using chicken breast as tissue imitation.	94
LaF_3:Yb^{3+},Nd^{3+}; LaF_3: Yb^{3+}@LaF_3:Nd^{3+}; LaF_3: Nd^{3+}@LaF_3:Yb^{3+}	Nd^{3+}, Yb^{3+}	790	LIR = 1350/1000	S = 0.41% °C^{-1} at 10 °C	10–50	LIR	Different types of core@ shell NPs were compared.	Researchers investigated how active-core/active-shell structures can serve as ratiometric thermal sensors to reveal fundamental properties of small animal tissues during *in vivo* experiments.	95
LaF_3:Yb^{3+}@LaF_3:Nd^{3+}	Nd^{3+}, Yb^{3+}	808	LIR = 1350/1000	S = 0.74% °C^{-1} at 20 °C	15–50	LIR		*Ex vivo* experiment showing the potential application of NPs for controlled photothermal subcutaneous treatments.	41
Ba_2LuF_7:Yb^{3+},Nd^{3+},Er^{3+}	Nd^{3+}, Yb^{3+}	808	LIR = 974/1052	0.63% °C^{-1} at 35 °C	35–255	LIR			96
$NaYbF_4$:Nd^{3+}@$NaYF_4$:Nd^{3+}	Nd^{3+}, Yb^{3+}	808	LIR = 1055/975	S = 0.7% °C^{-1}	20–220	LIR			97
$NaGdF_4$:Yb^{3+},Nd^{3+}	Nd^{3+}, Yb^{3+}	808	1012	1.59% °C^{-1} at 70 °C	30–70	Lifetimes			98
$NaYF_4$@$NaYF_4$:Yb^{3+},Nd^{3+}@CaF_2	Nd^{3+}, Yb^{3+}	808	1000	1.4% °C^{-1} at 10 °C	10–65	Lifetimes		Lifetime-based nanothermometers were tested *in vivo* for mapping the temperature distribution profile of the NP-interrogated area.	99

Table 1 (*continued*)

Type of nanoparticles	Emmiter	λ_{ex} (nm)	Emission bands used (nm)	Reported max. sensitivity	Reported *T*-range (°C)	Sensing parameter	Comments	Bioapplications in real conditions	Ref
$NaYF_4$@$NaYF_4$:Yb^{3+},Nd^{3+}@CaF_2	Nd^{3+}, Yb^{3+}	800	980	1.3% $°C^{-1}$ at 37 °C	20–60	Lifetime	Light to heat generation under continuous irradiation; pulsed excitation was used to monitor temperature.		100
$KLu(WO_4)_2$:Tm^{3+},Ho^{3+}	Tm^{3+}, Ho^{3+}	808	LIR_1 = 1480/1711; LIR_2 = 1711/1960	S_1 = 0.61% $°C^{-1}$; S_2 = 0.52% $°C^{-1}$ at 22 °C	22–62	LIR		*Ex vivo* temperature sensing experiments using chicken breast.	66
$KLu(WO_4)_2$:Ho^{3+},Tm^{3+}	Tm^{3+}, Ho^{3+}	808	LIR_1 = 1450/1960 LIR_2 = 1800/1960	S_1 = 0.9% $°C^{-1}$; S_2 = 0.19–0.9% $°C^{-1}$ at 20 °C	20–60	LIR	Different concentrations of Ho^{3+} and Tm^{3+} dopants were tested		74
$LiErF_4$:Ce^{3+}@$LiYF_4$	Er^{3+}	793	LIR = (1450–1580)/(1580–1650)	S = 0.40% $°C^{-1}$ at 20 °C	20–45	LIR			101
$NaNdF_4$:Yb^{3+}@$NaYF_4$ and $NaErF_4$@$NaYF_4$ mixed NPs	Er^{3+},Yb^{3+}	808	LIR = 1532/975	S = 3.1% $°C^{-1}$ at 20 °C	20–120	LIR	A mixture of two NPs types was used, showing the opposite behaviour of emission bands with increasing temperature.		102
Y_2O_3:Yb^{3+},Er^{3+},Ho^{3+}	Er^{3+} and Ho^{3+}	905	LIR = 1530/1200	S = 1.5% $°C^{-1}$ at 36 °C	25–200	LIR	Yb^{3+} to Er^{3+} and Ho^{3+} ET allowed for emission above 1000 nm.		103
$LuVO_4$:Yb^{3+}/Er^{3+}@SiO_2	Er^{3+}	915	LIR = 1496/1527	0.18% $°C^{-1}$	30–80	LIR	915 nm laser was used Instead of the 975 nm for Yb^{3+} ions excitation.		104
CaF_2:Yb^{3+},Er^{3+},Tm^{3+}	Er^{3+} and Tm^{3+}	940	1618, 1675, 1725 and 1812	$\Delta T \approx$ 0.75 °C	33–57	—	The authors used singular value decomposition analysis to determine the properties of the nanothermometer.		75
$LiYbF_4$:Er@$LiYF_4$	Er^{3+}	980	LIR between Stark levels within the 1425–1650 nm range	S = 0.248% $°C^{-1}$ at 25 °C	25–225	LIR			105

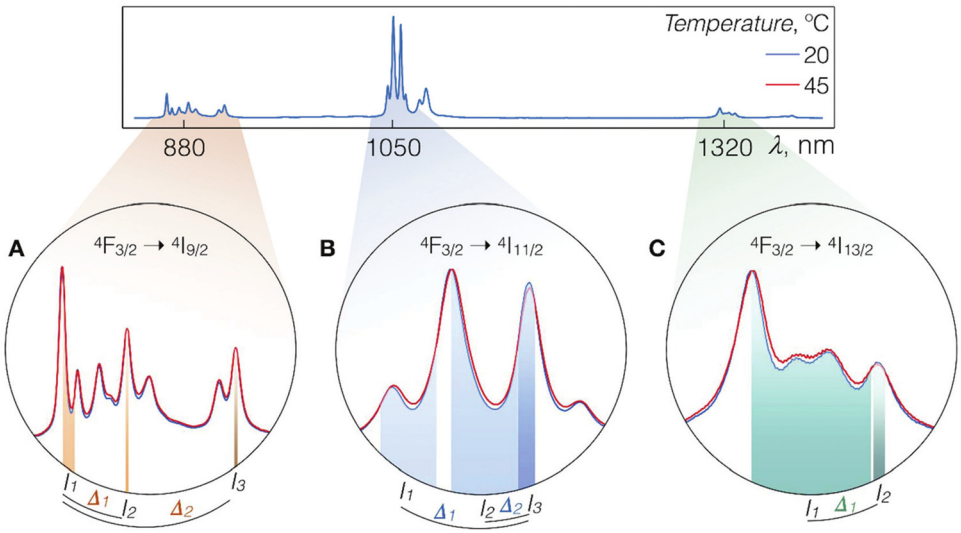

Fig. 2 Luminescence spectra of $LiLuF_4:Nd^{3+}$@$LiLuF_4$ at 20 and 45 °C with close-ups on the Nd^{3+} emission bands corresponding to A – $^4F_{3/2} \rightarrow {}^4I_{9/2}$, B – $^4F_{3/2} \rightarrow {}^4I_{11/2}$, and C – $^4F_{3/2} \rightarrow {}^4I_{13/2}$ radiative transitions. Shaded areas represent integration ranges from which intensity values I_n and I_m (n, m = 1, 2, and 3) can be used for calculations of thermometric parameters Δ_k (k = 1, or 2). Used with permission of The Royal Society of Chemistry, from ref. 59; permission conveyed through Copyright Clearance Center, Inc.

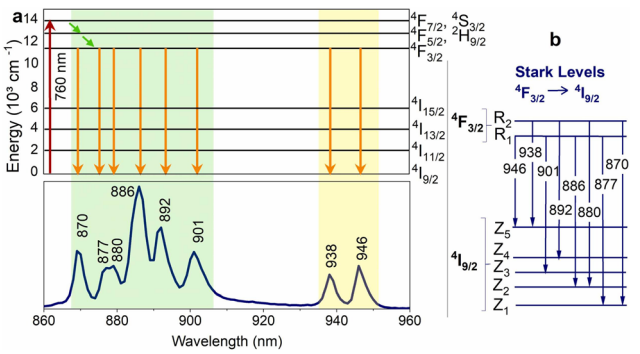

Fig. 3 (a) Nd^{3+} partial energy level diagram illustrating the excitation (760 nm) and relaxation pathways. The bottom part of the figure shows the corresponding emission spectrum of $Y_3Al_5O_{12}:Nd^{3+}$ NPs. (b) Representation of the Stark levels of the Nd^{3+} manifolds $^4F_{3/2}$ and $^4I_{9/2}$, as well as the electronic transitions associated with the emission peaks in the lower part of Fig. 3a.[82]

laser. The ratio between sub-bands at 885 and 863 nm shows temperature dependence, which the researchers tested in the 30–60 °C range. In this work, the authors also demonstrated phantom tissue penetration depth close to 2 mm. The thermal resolution in the tested tissue was determined to be ±2 °C. Better results in terms of thermal resolution, tested *ex-vivo*, were received by Rocha *et al.*[78] with a similar approach mentioned above based on LIR of the Stark-sublevels of Nd^{3+} ions. The researchers also studied $LaF_3:Nd^{3+}$ NPs, but in this case, they introduced additional annealing after the synthesis, which improved relative sensitivity and allowed for temperature resolution as low as 0.7 °C.[78] Carrasco *et al.*[83] developed a nanothermometer based on the $LaF_3:Nd^{3+}$ NPs by using emission lines at 865 and 885 nm, as well. Additionally, the NPs were tested as nanoheaters, proving that the $LaF_3:Nd^{3+}$ NPs can act simultaneously as light-to-heat converters (optical heaters) and temperature sensors. The same approach, *i.e.* the use of Nd^{3+} emission bands within the 860–890 nm range for LIR calculations, was used by Kolesnikov *et al.*,[56] who studied $YVO_4:Nd^{3+}$ NPs spectroscopic behaviour as a function of temperature. Interestingly, scientists were able to detect the emission of Nd^{3+} ions in the conducted *ex vivo* experiment from a depth of up to 1 cm.[56] Marciniak *et al.*[57] analysed the temperature effects on the luminescence of $LiNdP_4O_{12}$ nanocrystals in the 866–871 nm range, *i.e.* the LIR of the Stark components of the $^4F_{3/2} \rightarrow {}^4I_{9/2}$ transition band, receiving relative sensitivity of such nanothermometer around 0.22% °C^{-1} and temperature resolution 1.13 °C.[57] Because the studied NPs were highly doped with Nd^{3+} ions, the researchers also investigated photoinduced colloid temperature changes based on the obtained NPs. In another paper, Marciniak *et al.*[80] investigated the $NaNdF_4$@$NaYF_4$@$NaYF_4:Nd^{3+}$ NPs for temperature sensing and light-to-heat conversion. The authors of this work used the emission of Nd^{3+} ions under 808 nm, *i.e.*, two bands originating the two Stark levels of $^4F_{3/2}$ excited state, to determine the influence of temperature on the obtained LIRs. However, what distinguishes these results from others is that researchers also studied the dependence of LIRs on the power density of an exciting 808 nm laser, revealing some limitations of using Stark components of the $^4F_{3/2}$ level of Nd^{3+} ions at high excitation powers and the presence of efficient photothermal conversion even at low excitation powers. Huang *et al.*[81] tested $LiLuF_4:Nd^{3+}$ NPs for nanothermometry by using the same Nd^{3+} bands, *i.e.* 862/866 nm, but in a low temperature range, not covering typical biological temperature values. However, thanks to these studies, it was possible to discover that at very low temperature, in this case at −196 °C, the relative sensitivity exceeds the values reported elsewhere for the used LIR and it was 0.62% °C^{-1}.[81]

The emission lines at around 863–865 nm and 868–872 nm related to the $^4F_{3/2} \rightarrow {}^4I_{9/2}$ transition of Nd^{3+} ions are commonly used for temperature sensing, as indicated in the above paragraph. However, besides the intensity ratio, also their spectral position and FWHM can be used for temperature sensing, as proved by another work by Marciniak *et al.*[84] in their comprehensive studies on the influence of Nd^{3+} concentration and type of alkaline ions in the $ALaP_4O_{12}$ (A = Li, K, Na, Rb) host compound on the sensitivity of nanothermometers. From the presented research, it is clear that $R_1 \rightarrow Z_1$ and $R_2 \rightarrow Z_1$ Stark components of the Nd^{3+} $^4F_{3/2} \rightarrow {}^4I_{9/2}$ transition, *i.e.* the spectral position of the emission peaks connected with them, as well as their FWHM are strongly influenced by the crystal field of the host material and Nd^{3+}–O^{2-} distance. Hence, the absolute sensitivities of Nd^{3+}-based nanothermometers are also host-dependent, leading to *e.g.* variations between 0.17% $^\circ C^{-1}$ and 0.47% $^\circ C^{-1}$. However, from the presented studies, also another conclusion is drawn, *i.e.* nanothermometers based on the band position and FWHM can be good alternatives to those based on LIRs. The researchers reported that in all studied samples, sensitivities based on LIR were of lower values than those based on FWHM, and in low-doped samples, also on band position.[84]

In another study by Ortgies *et al.*,[8] the $^4F_{3/2} \rightarrow {}^4I_{9/2}$ emission band was successfully applied to monitor temperature in magnetic-luminescent polymer nanohybrids, which, besides optical heating, could also be used in magnetic-induced heating for hypothermia treatments. The studied hybrids consisted of LaF_3:Nd^{3+} and Fe_3O_4 NPs. By analysing the temperature behaviour of LIRs between Stark sublevels of $^4F_{3/2} \rightarrow {}^4I_{9/2}$ transition, *i.e.* the ratio between Nd^{3+} peaks at 862.5 and 864 nm under 808 nm excitation, the researchers revealed a nanothermometer with relatively high sensitivity of 0.4% $^\circ C^{-1}$.[8]

A similar approach was applied by Lozano-Gorrín *et al.*[77] in their studies on Nd^{3+}-doped $Y_3Ga_5O_{12}$ nanogarnets. The emission of Nd^{3+} ions under 808 nm excitation in the 860–940 nm range, related to $^4F_{3/2} \rightarrow {}^4I_{9/2}$ transition, was analysed in the 22–73.5 °C range. The Stark levels related to the $^4F_{3/2}$ multiplet undergo thermalization under 808 nm laser excitation, which causes the most significant changes of the bands in the 870–873.5 nm and 879.75–886.7 nm ranges. The ratio between these bands is temperature-sensitive and can be fitted to the Boltzmann distribution, giving rise to a thermal sensitivity of 0.13% $^\circ C^{-1}$ at 77 °C, with temperature resolution of ±2 °C.[77] Much higher sensitivity (0.34% $^\circ C^{-1}$ at 37 °C) was determined by Chen *et al.*[76] by measurements of Ni_2SiO_5:Nd^{3+} NPs under 808 nm excitation. The scientists were able to observe emission from Nd^{3+} ions at 850–1400 nm range, but for nanothermometry purposes, they used only $^4F_{3/2} \rightarrow {}^4I_{9/2}$ transition band and LIR between peaks at 863–873 nm and 896–901 nm.

Nanogarnet doped with Nd^{3+} ions was the subject of studies published by Dantelle *et al.*,[86] which, under 806 nm excitation, could observe luminescence from $Gd_3Sc_2Al_3O_{12}$:Nd^{3+} NPs with typical for Nd^{3+} emission bands at around 850–950 nm, 1060 nm and 1340 nm. The researchers used two peaks with maxima at 936 and 946 nm to determine the LIR between them as a function of temperature. These peaks are related to the emission of Nd^{3+} ions, *i.e.*, transitions from the $^4F_{3/2}$ to the highest component of the $^4I_{9/2}$ ground state of Nd^{3+} ions. The $^4F_{3/2}$ excited state of Nd^{3+} ions is split in the $Gd_3Sc_2Al_3O_{12}$ structure to two Stark sublevels separated by an energy gap equal to 113 cm^{-1}. Therefore, these two peaks are thermally-coupled and they are ruled by the Boltzmann distribution, which was used to calculate the thermal sensitivity of the nanothermometer, being around 0.21% $^\circ C^{-1}$ at room temperature (RT).[86] A similar approach was used by Benayas *et al.*[85] and Cantarano *et al.*[69] in Nd^{3+}-doped $Y_3Al_5O_{12}$ nanogarnets. The researchers also applied LIR of two emission bands at 938 and 945 nm related to transitions from Stark-levels of $^4F_{4/2}$ excited state to the highest component of $^4I_{9/2}$ ground state of Nd^{3+} ions. The relative sensitivities of such nanothermometers were like those mentioned above, *i.e.* around 0.15% $^\circ C^{-1}$ [85] or 0.20% $^\circ C^{-1}$,[69] which are typical values for the applied technique.

An interesting approach to temperature sensing *via* luminescence of Nd^{3+} ions under 808 nm laser irradiation was published by Kolesnikov *et al.*[64] In this study, YVO_4:Nd^{3+} NPs were selected as a temperature sensor with excitation and emission in the NIR range, operating within the 1st and 2nd BWs. Nd^{3+} ions show emission bands at around 1063.9 and 1071.1 nm related to the $^4F_{3/2} \rightarrow {}^4I_{11/2}$ transition (see Fig. 4, which shows the Stark levels related to this transition). The intensity ratio between these bands, spectral line positions and line bandwidth are temperature-dependent. The highest thermal sensitivity was determined for the method based on emission peak shift reaching up to 0.75% $^\circ C^{-1}$ at 30 °C. Quintanilla *et al.*[58] used the same approach, *i.e.* emission of Nd^{3+} in the 1050–1100 nm range when excited by 808 nm, to determine if CaF_2:Nd^{3+},Y^{3+} NPs are good candidates for nanothermometry based on LIR. The researchers used the intensity ratio between the sub-bands of $^4F_{3/2} \rightarrow {}^4I_{11/2}$ transition at 1053 and 1062 nm. The developed nanothermometer was characterized by typical sensitivity for this approach around 0.18% $^\circ C^{-1}$ at 22 °C.[58] In this work, also penetration depth, allowing for observation of NPs luminescence, was studied. The signal from the resulting NPs could be detected from as deep as 7 mm of chicken breast tissue. The sub-bands of Nd^{3+} $^4F_{3/2} \rightarrow {}^4I_{11/2}$ transition, but with maxima at 1060 and 1090 nm, were applied for nanothermometry purposes by Renero-Lecuna *et al.*,[89] in studies reporting LaOCl:Nd^{3+} and LaOCl:Nd^{3+}@LaOCl NPs. The authors of this report also presented comprehensive studies on the effects of Nd^{3+} ions concentration with the conclusion that relative sensitivity, which was around 0.25% $^\circ C^{-1}$ at 27 °C, and did not change at various concentrations of dopant ions.

Another example utilizing the luminescence of Nd^{3+} ions but with a different approach, *i.e.* using emission bands at 1060 and 1340 nm, was presented in the article by Silva *et al.*[87] (see Fig. 4 for more details regarding Nd^{3+} electronic transitions in this range). The reported TiO_2:Nd^{3+} NPs showed typical luminescence within the 850–1550 nm range, but the researchers decided to use only bands related to $^4F_{3/2} \rightarrow {}^4I_{11/2}$ and $^4F_{3/2} \rightarrow {}^4I_{13/2}$ although the $^4I_{13/2}$ level is not sensitive to temperature changes according to another report.[90] The researchers also studied the effects of the annealing temperature of products on the final relative sensitivities. The maximum sensitivity was 0.82% $^\circ C^{-1}$ at 27 °C for products obtained at 100 °C.

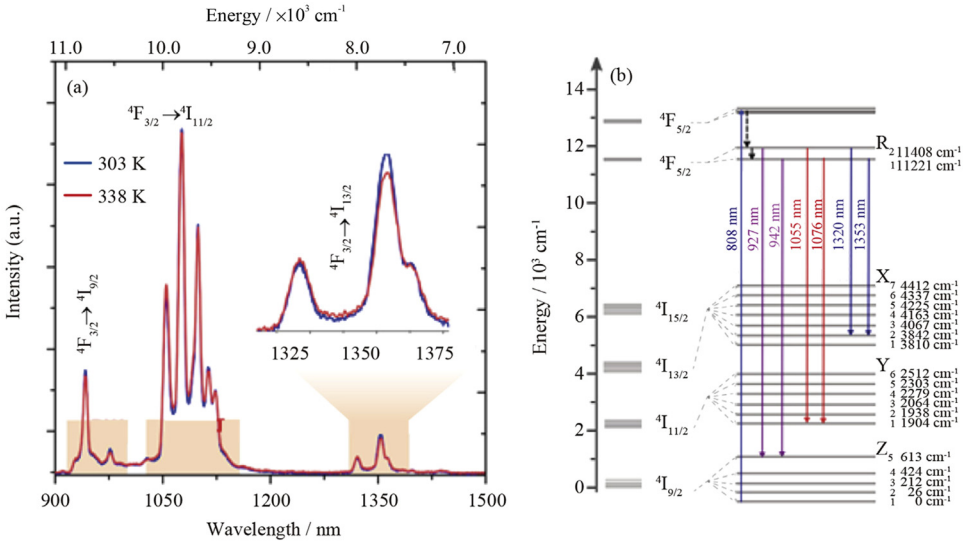

Fig. 4 (a) NIR emission spectra of $(Gd_{0.98}Nd_{0.02})_2O_3$ NPs in Dulbecco's modified Eagle's medium at 25 and 65 °C. The shaded regions depict 1st, 2nd and 3rd BWs; (b) partial energy level diagram of Nd^{3+} ions showing the transitions used for defining the thermometric parameters.[72]

The temperature changes of emission bands related to $^4F_{3/2} \rightarrow {}^4I_{13/2}$ transition were analysed in detail by Balabhadra *et al.*[90] in Gd_2O_3:Nd^{3+} NPs. The emission band under 808 nm excitation in the 1250–1550 nm range usually comprises several components due to the crystal field splitting (see Fig. 5). The researchers identified bands related to each Stark-level by deconvoluting the recorded emission. They thereby revealed that the emission associated with the electron transition between the higher-energy state component $^4F_{3/2}$ and the components of the $^4I_{13/2}$ level is not sensitive to temperature changes, in contrast to the transitions from the lower-energy state component of $^4F_{3/2}$. They reported maximum thermal sensitivity equal to 0.23% °C^{-1} at 30 °C.

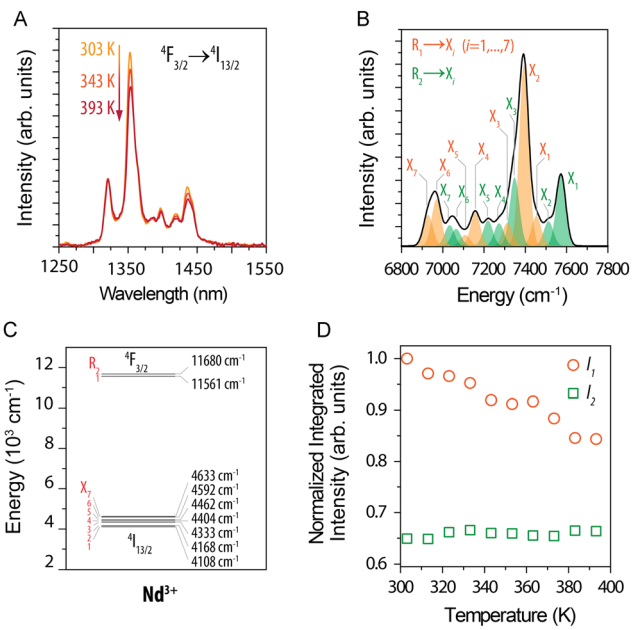

Fig. 5 (A) Part of emission spectra of $(Gd_{0.972}Nd_{0.028})_2O_3$ NPs recorded in the 30–120 °C (303–393 K) range under 808 nm excitation. (B) Deconvoluted emission spectrum obtained at 50 °C (323 K). (C) Simplified energy level diagram. (D) Normalized integrated intensity of I_1 (orange circles) and I_2 (green squares). Reprinted from ref. 90; Copyright (2016), with permission from Elsevier.

Excellent work summarizing different methods for ratiometric temperature sensing was demonstrated by Gschwend *et al.*,[71] who presented how the choice of Nd^{3+} emission bands for LIR can affect the thermal sensitivities within the 1st and 2nd BW. The researchers used 750 nm laser radiation instead of 808 nm to excite Nd^{3+} ions in the $BiVO_4$ NPs, thanks to which they could observe an emission band with a maximum at around 820 nm, correlated with the $^4F_{3/2} \rightarrow {}^4I_{9/2}$ transition. Therefore, it was possible to calculate the dependence of the ratio between $^4F_{5/2} \rightarrow {}^4I_{9/2}$ and $^4F_{3/2} \rightarrow {}^4I_{9/2}$ or $^4F_{3/2} \rightarrow {}^4I_{11/2}$ transition bands (at 870 or 1064 nm, respectively) on temperature. Usually, in Nd^{3+}-based nanothermometers, the intensity between Stark components of transitions at 860–925 nm and 1050–1100 nm are taken for LIRs calculation.[64,65,86] However, in the reported work, the authors proved that due to the small energy differences between Stark levels ($\Delta E < 300$ cm^{-1}), the reported sensitivities are usually low in the 0.1–0.3% °C^{-1} range. By taking advantage of 750 nm excitation and the possibility of observing the additional emission peak at 820 nm and the significant energy differences between bands employed for LIRs calculations, the researchers could obtain nanothermometers with up to 1.53% °C^{-1} sensitivity.[71] What is more, the researchers proved the potential of $BiVO_4$:Nd^{3+} nanothermometer for deep-tissue thermal sensing in *ex vivo* experiments with chicken tissue.

Meaningful work for Nd^{3+}-based nanothermometry under 808 nm was also published by Rakov *et al.*,[93] who compared how the selection of different emission bands for LIR calculations influences the sensitivity of thermometers. The researchers used Y_2O_4:Nd^{3+} NPs and emission lines related to $^4F_{3/2} \rightarrow {}^4I_{9/2}$ (900–950 nm), $^4F_{3/2} \rightarrow {}^4I_{11/2}$ (1050–1150 nm) and $^4F_{3/2} \rightarrow {}^4I_{13/2}$ (1300–1450 nm) transitions (see Fig. 5). According to the results

obtained, the 942/935 nm and 1100/1084 nm LIRs provide the highest sensitivity of around 0.45% $^{\circ}C^{-1}$.[93] Kolesnikov *et al.*[91] analysed Y_2O_3:Nd^{3+} NPs similarly, concluding that 1053/1075 nm LIR give the best relative sensitivity of 0.47% $^{\circ}C^{-1}$ (by studying 25–60 °C range). An analogous comparison published by Debasu *et al.*[72] proved that the 927/942 nm LIR gives the best relative sensitivity, which in their case reached 2.18% $^{\circ}C^{-1}$ at 25 °C by using Gd_2O_3:Nd^{3+} NPs.

One of the best works in the field of nanothermometry using Nd^{3+} ions was published by Skripka *et al.*[59] In this study, scientists analysed all possible options for observation within the BW of the emission spectrum of Nd^{3+} ions under the influence of 793 nm laser irradiation (all bands at around 880, 1050 and 1320 nm). The luminescence of $LiLuF_4$:Nd^{3+}@$LiLuF_4$ NPs at approximately 1050 nm, corresponding to the $^4F_{3/2} \rightarrow {}^4I_{11/2}$ transition, emerged as the most suitable option for thermal readout. Its effectiveness was presented in measuring transient temperatures during subcutaneous *ex vivo* experiments. Although the luminescence at around 1320 nm ($^4F_{3/2} \rightarrow {}^4I_{13/2}$) was deemed unsuitable for temperature sensing, it presented an advantageous use in NIR optical imaging. The highest sensitivity determined in the presented study was 0.58% $^{\circ}C^{-1}$ at 20 °C.[59]

2.2. Nanoparticles doped with Nd^{3+} ions and co-doped with another Ln^{3+} ions excitable under 808 nm laser radiation

The nanothermometers based on ET from Nd^{3+} ions, effectively absorbing radiation at around 808 nm, to other Ln^{3+} ions can provide additional emission bands within BW, which can be used for LIR calculation. Nd^{3+} to Er^{3+} ET was adopted by Maciejewska *et al.*[92] in $LaPO_4$ NPs for remote temperature sensing using down-shifted luminescence of Nd^{3+} at 1300 nm ($^4F_{3/2} \rightarrow {}^4I_{13/2}$) and Er^{3+} at 1540 nm ($^4I_{13/2} \rightarrow {}^4I_{15/2}$). The researchers determined that the LIR of these bands highly depends on the Er^{3+} dopant concentration. The highest sensitivity of 1.15% $^{\circ}C^{-1}$ at 267 °C was observed for $LaPO_4$:1%Nd^{3+},20%Er^{3+} NPs. In the biological *T*-range, the sensitivity was around 0.5% $^{\circ}C^{-1}$. The ET mechanism and emission spectra related to this research are presented in Fig. 6.

In the article mentioned above,[92] regarding $LaPO_4$:Nd^{3+},Er^{3+} NPs, the researchers also applied another way of remote temperature sensing, based on luminescence decays of Nd^{3+} at 1055 nm ($^4F_{3/2} \rightarrow {}^4I_{11/2}$). Because the $Nd^{3+} \rightarrow Er^{3+}$ ET requires phonon assistance, it is affected by temperature and depends on the Er^{3+} concentration. The revealed sensitivity of $LaPO_4$:1%Nd^{3+},5%Er^{3+} NPs was 2.3% $^{\circ}C^{-1}$ at 54 °C. The results indicate that the luminescence lifetime-based $LaPO_4$:Er^{3+},Nd^{3+} nanothermometer has substantial potential for practical applications within the temperature range of 227–327 °C, which is above the biological *T*-range. However, the presented method may apply to other NPs designed for bioapplications.

Emission bands of both Nd^{3+} and Yb^{3+} ions were adapted for temperature sensing in the studies provided by Ximendes *et al.*,[95] in which the researchers compared three types of Nd^{3+}-doped NPs, *i.e.* LaF_3:Yb^{3+},Nd^{3+}, LaF_3:Yb^{3+}@LaF_3:Nd^{3+} and LaF_3:Nd^{3+}@LaF_3:Yb^{3+}. The studied NPs could emit in the 900–1400 nm range upon excitation with a 790 nm laser. The changes of the intensity ratio between Nd^{3+} emission at around

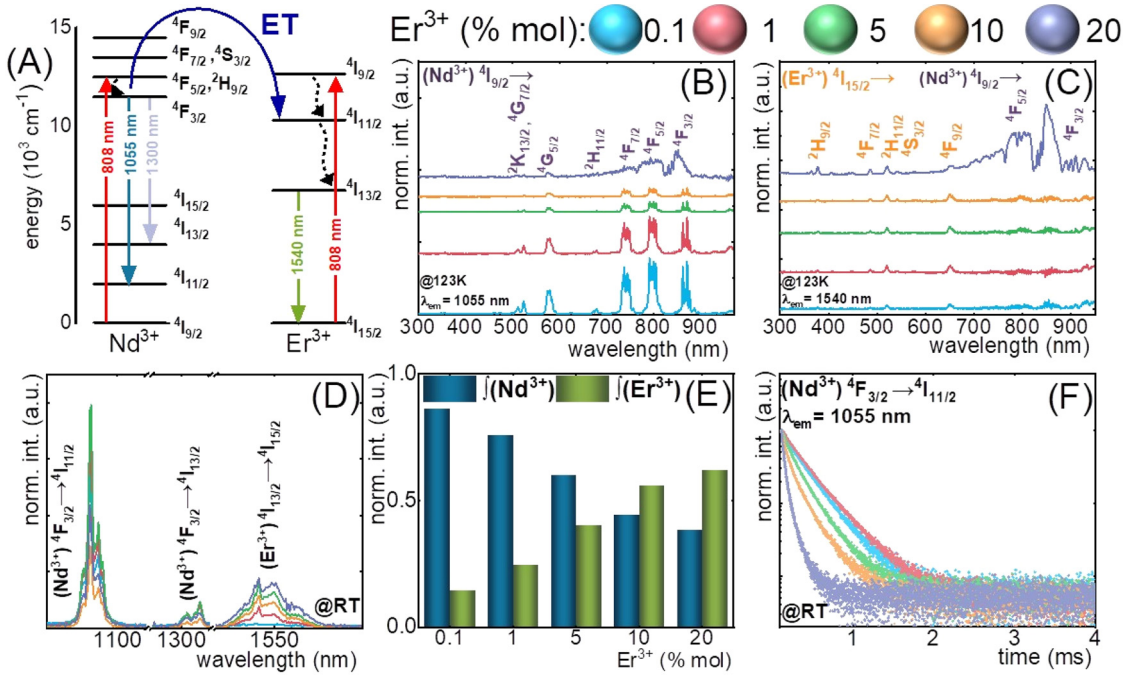

Fig. 6 (A) The simplified energy diagrams of Er^{3+} and Nd^{3+} ions in $LaPO_4$ nanocrystals; (B) and (C) the representative excitation spectra of $LaPO_4$:Er^{3+},Nd^{3+} nanocrystals measured at −150 °C (123 K) for Nd^{3+} (λ_{em} = 1055 nm) and Er^{3+} (λ_{em} = 1540 nm); (D) the comparison of the room temperature emission spectra of $LaPO_4$:Er^{3+},Nd^{3+} nanocrystals for different Er^{3+} concentrations; (E) relative integral emission intensities of Nd^{3+} ($^4F_{3/2} \rightarrow {}^4I_{11/2}$) and Er^{3+} ($^4F_{13/2} \rightarrow {}^4I_{15/2}$) ions for different Er^{3+} concentration measured at room temperature and (F) the room-temperature luminescence decay profiles of $^4F_{3/2}$ state of Nd^{3+} ions for different Er^{3+} concentrations.[92]

1350 nm ($^4F_{3/2} \rightarrow {}^4I_{13/2}$) and Yb^{3+} at 1000 nm ($^2F_{5/2} \rightarrow {}^2F_{7/2}$) were determined in the 10–50 °C range, allowing for calculation of relative sensitivities. The highest sensitivity (0.41% $°C^{-1}$) was obtained for the LaF_3:Nd^{3+}@LaF_3:Yb^{3+} NPs. The study also presented *in vivo* experiments using the obtained NPs on small animals. The same group of researchers published similar results on LaF_3:Yb^{3+}@LaF_3:Nd^{3+} using Yb^{3+} and Nd^{3+} luminescence at 1000 and 1350 nm but with the focus on simultaneous heating and thermal feedback studied *ex vivo*.[41] The researchers used a higher concentration of Nd^{3+} ions to induce heating of the NPs under 808 nm laser excitation.

Yb^{3+} and Nd^{3+} emission bands for luminescence thermometry were also used in another work published by Li *et al.*[96] Under excitation with 808 nm, the Ba_2LuF_7:Yb^{3+},Nd^{3+},Er^{3+} NPs presented several emission peaks within 900–1600 nm range, but the authors of the article used two bands with maxima at 974 and 1052 nm for calculation how the LIR between these bands change with temperature in the 35–255 °C range. The first peak corresponds to the Yb^{3+} $^2F_{5/2} \rightarrow {}^2F_{7/2}$ transition, whereas the second is to the Nd^{3+} $^4F_{3/2} \rightarrow {}^2I_{11/2}$ transition. The reported sensitivity of this system was 0.63% $°C^{-1}$ at 35 °C.

Ji *et al.*[98] instead of measuring the emission of Yb^{3+} in the Nd^{3+}/Yb^{3+} system, decided to determine how the Yb^{3+} luminescence decay times change with temperature when $NaGdF_4$:Yb^{3+},Nd^{3+} NPs are excited *via* an 808 nm pulsed laser. The tested NPs presented high relative sensitivity in the 30–70 °C range, reaching a maximum of 1.59% $°C^{-1}$ at 70 °C.

Lifetime-based nanothermometry utilizing Nd^{3+} to Yb^{3+} ET was also proposed by López-Peña *et al.*[100] The researchers demonstrated $NaYF_4$@$NaYF_4$:Yb^{3+},Nd^{3+}@CaF_2 NPs capable of conversion of 800 nm pulsed laser excitation into Yb^{3+} emission at 980 nm, with luminescence decay times sensitive to temperature changes, reporting a relative sensitivity of 1.3% $°C^{-1}$ at 37 °C. What is more, the studies show that using 800 nm continuous excitation results in heating, contrary to pulsed excitation. The researchers demonstrated a scheme for simultaneous heating and temperature detection, an interesting and new path for developing *in vivo* treatments. Wu *et al.*[62] also used Yb^{3+} lifetimes at 980 nm as temperature-sensitive parameter in $NaYF_4$@$NaYF_4$:Yb^{3+},Nd^{3+}@$NaYF_4$ NPs under excitation with 808 nm laser. They obtained a similar to the sensitivity mentioned above of 1.54% $°C^{-1}$ at 55 °C. Similar results, *i.e.* sensitivity 1.4% $°C^{-1}$ at 10 °C, using Yb^{3+} luminescence decay kinetics (excited state lifetimes) as temperature change indicator, were obtained by Tan *et al.*[99] The researchers investigated $NaYF_4$@$NaYF_4$:Yb^{3+},Nd^{3+}@CaF_2 NPs, also including experiments *in vivo* to demonstrate the applicability of tested nanothermometers.

The disadvantage of the above-discussed Yb^{3+}/Nd^{3+}-based nanothermometers is that the absorption maximum of Yb^{3+} ions and part of their emission falls out of the BWs. However, the reported data suggest that the signal from the Yb^{3+} ions can be collected below 950 nm or above 1000 nm, similar to the approach presented by Runowski *et al.*,[51] who used a 900–950 nm/1000–1100 nm integration range to include emission of Yb^{3+} in the reported nanothermometers.

Nd^{3+}–Yb^{3+}–Er^{3+} system was applied by Liu *et al.* in core@shell@shell NPs to obtain luminescence of Er^{3+} ions with several peaks in the range of 1475–1626 nm under excitation *via* Nd^{3+} at 808 nm. The authors could detect energy transfer between shells, where Yb^{3+} ions acted as bridges connecting the absorbing shell with the emitting core. As a host compound, the researchers used $LiYF_4$ fluoride. The intensity of Er^{3+} emission peaks related to Stark sublevels are temperature sensitive; with increasing temperature, the higher Stark levels become populated according to the Boltzmann theory. Therefore, the authors could determine LIRs between the lower and higher excited states, but unfortunately, they limited their studies to only 980 nm excitation.[106]

A different approach also utilizing the emission of Er^{3+} ions was proposed by Wang *et al.*,[102] who used a mixture of two types of NPs excitable at 808 nm laser excitation, *i.e.* $NaNdF_4$:Yb^{3+}@$NaYF_4$ and $NaErF_4$@$NaYF_4$ NPs. Under laser excitation, the $NaNdF_4$:Yb@$NaYF_4$ NPs demonstrated emission at 975 nm, aligning with the Yb^{3+} $^2F_5/_2 \rightarrow {}^2F_{7/2}$. Simultaneously, the $NaErF_4$@$NaYF_4$ NPs exhibit noticeable emission at around 1532 nm, corresponding to the Er^{3+} $^4I_{13/2} \rightarrow {}^4I_{15/2}$ transition. Researchers observed that when the temperature increased, the emission intensity of Yb^{3+} decreased, while Er^{3+} ions increased, which allowed determining 1532/975 nm LIR and relative sensitivity at 30 °C equal to 3.1% $°C^{-1}$.[102]

An interesting approach to nanothermometry for biological applications was presented by Skripka *et al.*[55] by utilizing the multishelled properties of $NaGdF_4$-based NPs, with different compositions of each shell. The researchers synthesized NPs doped with Er^{3+}, Ho^{3+} and Yb^{3+} in the core, with Yb^{3+} in the subshell and Nd^{3+} and Yb^{3+} in the shell. Thanks to the advanced architecture of NPs, it was possible to observe emission bands of Ho^{3+} at 1180 nm ($^5I_6 \rightarrow {}^5I_8$ transition), Nd^{3+} bands at 1340 nm ($^4F_{3/2} \rightarrow {}^4I_{13/2}$) and Er^{3+} bands at around 1550 nm ($^4I_{13/2} \rightarrow {}^4I_{15/2}$) under excitation with 806 nm laser (see Fig. 7 for more details). The luminescent properties of the NPs allowed for LIR calculations within the 2nd or both 2nd and 3rd BWs. The luminescence of multishelled $NaGdF_4$ NPs was recorded within the 20–50 °C range, allowing to determine relative sensitivities to approximately 1.1% $°C^{-1}$ by taking the Ho^{3+}/Nd^{3+} or Er^{3+}/Nd^{3+} emission bands for calculations. The researchers also estimated the temperature uncertainty around 1.2 and 0.8 °C for LIR (Ho^{3+}/Nd^{3+}) and LIR (Er^{3+}/Nd^{3+}), respectively. A similar approach, *i.e.* utilizing Nd^{3+} ions as emission sensitizers for 808 nm excitation and Ho^{3+} and Er^{3+} ions as emitters, was presented in the study by Xu *et al.*[94] The LIR between $^5I_6 \rightarrow {}^5I_8$ emission band of Ho^{3+} ions at 1164 nm and $^4I_{13/2} \rightarrow {}^4I_{15/2}$ emission band of Er^{3+} at 1534 nm showed temperature dependence with 0.88% $°C^{-1}$ or 1.30% $°C^{-1}$ relative sensitivity at 55 °C depending on the architecture of the core@shell NPs.

Excitation at 808 nm and ET, CR processes between Ln^{3+} dopant ions were applied in another study reporting sophisticated core@shell@shell structures, *i.e.* $NaGdF_4$:Yb^{3+},Tm^{3+}@$NaYF_4$:Yb^{3+}@$NaGdF_4$:Yb^{3+},Nd^{3+}@$NaGdF_4$ NPs to obtain emission bands within the 2nd BW for nanothermometry.[73] Hu *et al.* in this study observed emission at 1215 nm from Tm^{3+} ions related to $^3H_5 \rightarrow {}^3H_6$ transition, which was used as a reference, and emissions at 1330 and 1470 nm from $^3F_{3/2} \rightarrow {}^4I_{13/2}$

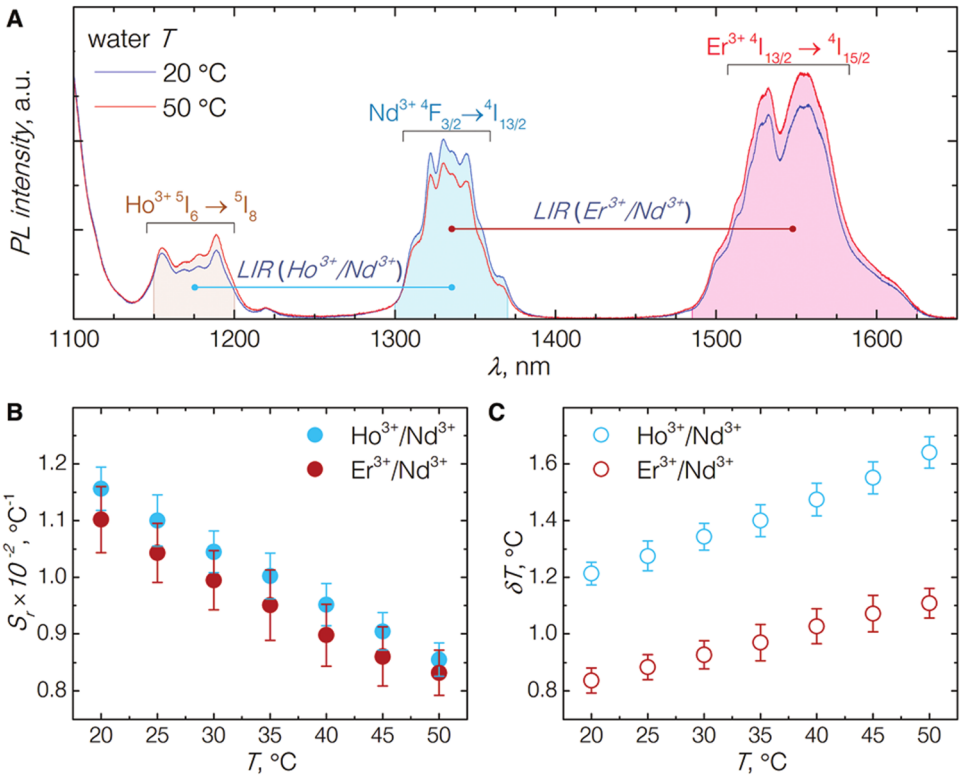

Fig. 7 (A) Emission spectra of $NaGdF_4$:Er^{3+},Ho^{3+},Yb^{3+}@$NaGdF_4$:Yb^{3+}@$NaGdF_4$:Nd^{3+},Yb^{3+} NP under excitation by 806 nm laser; emission intensity integration ranges for each band are shown as shaded areas underneath the curves. (B) The relative thermal sensitivities for both NIR emission band pairs. (C) The temperature uncertainties estimated from the temperature-dependent emission behaviour of the studied NPs. Used with permission of The Royal Society of Chemistry, from ref. 55; permission conveyed through Copyright Clearance Center, Inc.

transition of Nd^{3+} and $^3H_4 \rightarrow {}^3F_4$ transition of Tm^{3+} ions, employed as temperature-sensitive bands for ratiometric thermometers. Moreover, the researchers optimized their NPs for Tm^{3+} emission by utilizing the CR process between Gd^{3+} and Tm^{3+} ions. The maximum of the reported relative sensitivity was 1.07% $°C^{-1}$ at 30 °C for 1470 nm/1215 nm LIR.[73]

2.3. Nanoparticles doped with Tm^{3+} or Er^{3+} ions used as sensitizers for luminescence under 808 nm excitation

Another Ln^{3+} ion with great potential for applications based on excitation and emission within BW is Tm^{3+}. Its electronic structure allows for excitation at 808 and 1208 nm due to the $^3H_6 \rightarrow {}^3H_4$ and $^3H_6 \rightarrow {}^3H_5$ transitions, respectively.[107] Excitation *via* 808 nm laser radiation seems to be especially useful for down-shifted nanothermometers. Tm^{3+} may also act as a sensitizer for NIR radiation, transferring its energy to, *e.g.* Er^{3+} or Ho^{3+} ions.[66,108] An example of such a system is presented in Fig. 8.

Such an unusual system, in which the emission of various Ho^{3+} ions was used to monitor temperature, was proposed by Savchuk *et al.* in $KLu(WO_4)_2$:Tm^{3+},Ho^{3+} NPs.[66] Under 808 nm excitation, the studied NPs presented emission bands at 1480, 1711 and 1960 nm, which corresponded to $^3H_4 \rightarrow {}^3F_4$ and $^3F_4 \rightarrow {}^3H_6$ transitions of Tm^{3+} ions and $^5I_7 \rightarrow {}^5I_8$ transition of Ho^{3+} respectively. The researchers revealed that the 1480/1711 nm and 1711/1960 nm LIRs show the best relative sensitivity among other studied samples: 0.61% $°C^{-1}$ and 0.52% $°C^{-1}$, respectively, at 22 °C. Also, Tm^{3+} or Tm^{3+}–Yb^{3+}-doped systems were presented, but the sensitivities were much lower.[66] Similar results based on the same type of materials were obtained by Nexha *et al.*,[74] who also studied $KLu(WO_4)_2$:Tm^{3+},Ho^{3+} NPs (Fig. 8). The researchers revealed that by using 808 nm excitation it is possible to observe three main bands attributed to the electronic transitions of Tm^{3+} ions, *i.e.* $^3H_4 \rightarrow {}^3F_4$ (at 1450 nm) and $^3F_4 \rightarrow {}^3H_6$ (at 1800 nm) and Ho^{3+} ions, *i.e.* $^5I_7 \rightarrow {}^5I_8$ (at 1960 nm–out of the 3rd BW). Determined temperature-depended behaviour of 1450/1960 nm and 1800/1960 nm LIRs at 20–60 °C range allowed the calculation of relative sensitivities, from which the best was equal to 0.9% $°C^{-1}$ at 20 °C for both types of LIRs. In the presented research, different concentrations of Ho^{3+} and Tm^{3+} ions were tested, from which the most promising was 1% mol. of Ho^{3+} and 10% mol. of Tm^{3+} ions.[74]

Er^{3+} ions, thanks to their complex electronic structure, can be excited by several excitation wavelengths in the NIR range, *i.e.* 808, 975 and 1532 nm. Their versatile capabilities make them one of the best dopant ions in nanocarriers for biomedical applications.[54] Under excitation *via* 808 nm laser, Er^{3+} ions show down- and upconverting luminescence.[107] Hazra *et al.*,[101] investigated the effects of temperature on the luminescence of Er^{3+} ions in the 1475–1626 nm range by using 793 nm excitation. Er^{3+} ions can absorb the wavelength at around 800 nm, showing down-shifted emission in the 3rd BW range. The scientists studied $LiErF_4$:Ce^{3+}@$LiYF_4$ NPs, and two spectral

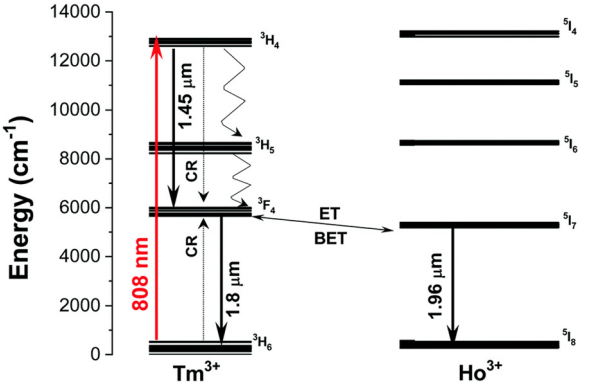

Fig. 8 Energy level diagram of Ho^{3+} and Tm^{3+} ions in $KLu(WO_4)_2$:Tm^{3+},Ho^{3+} NPs and the mechanisms of generation of their emission lines. Solid arrows indicate radiative processes and red arrows indicate the absorption process excited by the 808 nm laser. The curved arrows indicate non-radiative multiphonon decay processes. The dashed arrows stand for the cross-relaxation process between Tm^{3+} ions. Used with permission of The Royal Society of Chemistry, from ref. 74; permission conveyed through Copyright Clearance Center, Inc.

ranges were considered for the calculation of LIRs: 1450–1580 nm and 1580–1650 nm, within which the emission bands related to the $^4I_{13/2} \rightarrow {}^4I_{15/2}$ transition were located. Moreover, the researchers also investigated the effect of Ce^{3+} co-doping on the effectiveness of the nanothermometer, revealing that a small amount of Ce^{3+} ions (1%) enhanced its sensitivity. The determined relative sensitivity was 0.40% °C^{-1} at 20 °C.[101] Wang *et al.*,[102] whose results are discussed earlier in section 3.2, used $NaErF_4$@$NaYF_4$ NPs as the component of a mixture with $NaNdF_4$:Yb^{3+}@$NaYF_4$ NPs, which showed emission at around 1532 nm, corresponding to the Er^{3+} $^4I_{13/2} \rightarrow {}^4I_{15/2}$ transition under 808 nm excitation and used for the calculation of LIRs together with emission at 975 nm from the second component of the mixture.

2.4. NPs doped with Yb^{3+} ions as sensitizers and excitable within the 900–950 nm range

There are only a few publications utilizing excitation *via* Yb^{3+}, but not employing the typical wavelength of 975/980 nm for such systems, but rather 905 nm, as was published by Porosnicu *et al.*[103] or 915 nm reported by Xiang *et al.*[104] As known, radiation with a wavelength of around 975 nm is strongly absorbed by water, causing heating of the medium. On the other hand, 905–915 nm falls within the range of the 1st BW and can be applied in nanothermometry. The authors of the article mentioned above by Porosnicu *et al.* reported Y_2O_3:Yb^{3+},Er^{3+},Ho^{3+} NPs showing good relative sensitivity of 1.5% °C^{-1} at 36 °C. To achieve it, the researchers used LIR based on the emission of Er^{3+} ions at 1530 nm, related to the $^4I_{13/2} \rightarrow {}^4I_{15/2}$ transition and emission of Ho^{3+} ions at around 1200 nm connected with $^5I_6 \rightarrow {}^5I_8$ transition under 905 nm pulsed laser excitation. The observed down-shifted emission was possible due to the Yb^{3+} to Er^{3+} and Yb^{3+} to Ho^{3+} ETs. Also, preliminary studies *ex vivo* based on the obtained nanothermometer were presented. In the second article published by Xiang *et al.*[104] $LuVO_4$:Yb^{3+}/Er^{3+}@SiO_2 NPs were excited *via* 915 nm laser, and the intensity ratio between the Stark-components of Er^{3+} emission band at around 1530 nm related to the $^4I_{13/2} \rightarrow {}^4I_{15/2}$ transition was used for nanothermometry purposes. The reported relative sensitivity based on 1496/1527 nm LIR was lower than reported in the article mentioned above, *i.e.* 0.18% °C^{-1}.[104]

3. Upconverting nanothermometers

The upconversion phenomenon has been recently intensively investigated, mainly because of its high potential in biomedicine.[109–111] This is thanks to the possibility of using NIR excitation radiation, which is non-destructive for biological material and critical in bioimaging,[109] drug delivery[112] or photodynamic therapy.[111] Contrary to the down-shifting nanothermometers, upconverting ones allow for excitation in the 1st BW and further into the NIR, *i.e.* within the 2nd or even 3rd BW, with simultaneous emission at lower-frequency wavelengths (see Table 2). Additionally, excitation in the further infrared range of BW reduces the possibility of autofluorescence, making it practically impossible.

3.1. Excitation *via* Yb^{3+} ions in the 900–950 nm range

The Yb^{3+} ion exhibits a straightforward energy level structure characterized by just two multiplets. The first is the $^2F_{7/2}$ ground state, featuring four Stark levels, and the second is the $^2F_{5/2}$ excited state, which has three Stark levels. These two states are distinctly separated by a substantial energy gap, approximately 10 000 cm^{-1}. Furthermore, this ion displays a prominent, wide absorption band, peaking at around 975 nm. These properties of Yb^{3+} ions are used to sensitize UCNPs.[35] Due to the energy transfer between Yb^{3+} and other Ln^{3+} ions such as Er^{3+}, Ho^{3+} or Tm^{3+}, it is possible to observe bright anti-Stokes emission from these ions in the UV-NIR range. The problem with Yb^{3+} ions is that the maximum of their absorption is out of the 1st BW range, *i.e.* at around 970–980 nm, where water, on the other hand, strongly absorbs radiation and using excitation light close to 980 nm results in heating water-containing systems. Upconverting systems based on Yb^{3+} are usually characterized by intense emission and relatively high emission quantum yields.[116] However, it is possible to excite Yb^{3+} ions with radiation from the 1st biological window, which apparently is not frequently used.

Particularly interesting are the properties of Yb^{3+} ions in the garnet structure, *i.e.* high absorption coefficient for closely aligned peaks in the 920–945 nm range.[77] It allows for the excitation of Yb^{3+}/Er^{3+}-doped $Y_3Ga_5O_{12}$ garnet NPs *via* 920 nm laser radiation. Lozano-Gorrín *et al.*[77] used such a system to develop nanothermometers applicable to biological systems. In contradiction to the most studied Yb^{3+}/Er^{3+}-based nanothermometers, the researchers observed the temperature-dependent emission related to $^2H_{11/2} \rightarrow {}^4I_{13/2}$ and $^4S_{3/2} \rightarrow {}^4I_{13/2}$ transitions, which occurs within 780–870 nm range. The $^2H_{11/2}$ and $^4S_{3/2}$ excited states of Er^{3+} ions are thermally coupled, with around 800 cm^{-1} energy difference between them. The radiative relaxation process to the $^4I_{15/2}$ ground state of Er^{3+} ions is connected with the green emission of these ions, the most

Table 2 Nanothermometers based on photon upconversion

Type of nanoparticles	Emitter	Excitation (nm)	Emission bands for temperature sensing	Reported max. relative sensitivity	Reported temperature range (°C)	Technique	Comments/bioapplications in real conditions	Ref.
$Y_3Ga_5O_{12}$:Yb^{3+},Er^{3+}	Er^{3+}	920	LIR = (780–816)/(840–868)	S = 0.8% °C^{-1} at 77 °C	22–77	LIR		77
$NaYF_4$:Ho^{3+}@$NaYF_4$, $NaYF_4$:Ho^{3+},Er^{3+}@$NaYF_4$	Ho^{3+}, Er^{3+}	1151	LIR_1 = 648/898 (Ho^{3+}); LIR_2 = (648–672)/898 (Ho^{3+},Er^{3+})	S_1 = 0.66% °C^{-1} (Ho^{3+}); S_2 = 0.89% °C^{-1} (Ho^{3+}/Er^{3+})	22–105	LIR		113
$NaYF_4$:Tm^{3+},Er^{3+}@$NaYF_4$	Tm^{3+}, Er^{3+}	1028	LIR_1 = 982/698; LIR_2 = 982/802	S_1 = 2.37% °C^{-1} at 57 °C; S_2 = 1.58% °C^{-1} at 67 °C	21–115	LIR		108
$YAlO_3$:Tm^{3+}	Tm^{3+}	1210	LIR_1 = 705/800; LIR_2 = 796/801.5	S_1 = 0.26% °C^{-1} at 51 °C; S_2 = 0.12% °C^{-1} at 26 °C	21–152	LIR		114
$NaNbO_3$:Tm^{3+}	Tm^{3+}	1319	LIR = 797/807	S = 0.8% °C^{-1} at 30 °C	30–70	LIR	*Ex vivo* experiments on chicken pectoral muscle to analyse excitation and emission penetration depths	60
SrF_2:Er^{3+}	Er^{3+}	1532	LIR = 800/970	S = 0.93% °C^{-1} at 100 °C	0–100	LIR	Various concertinos of Er^{3+} ions were checked	115

studied in terms of optical thermometry. The authors proposed a different approach, opening the possibility of observing Er^{3+} temperature-dependent emission within the 1st BW.

3.2. 1151 nm excitation *via* Ho^{3+} ions

Excitation around 1151 nm fits the 2nd BW. Upconverting systems capable of emission under excitation at around 1151 nm base of absorption of the Ho^{3+} ions, which undergo excitation, by using this wavelength, from the $^5I_8$ ground state to the $^5I_6$, the second excited state.[113] Ho^{3+} ions due to the ground state absorption (GSA) followed by excited state absorption (ESA) or ET between Ho^{3+} ions can be excited up to their $^3F_3$ excited state, which results in the emission at 489 nm or, after relaxation, at 544 nm. However, the most important factor for nanothermometry in bioapplications is their emission within the 1st BW at around 648, 752 and 898 nm.

Studies reporting UCNPs under excitation close to 1151 nm are rare; only a single paper has been published in this area. Ryszczynska *et al.*[113] reported a $NaYF_4$-based core@shell nanothermometer where Ho^{3+} ions were used as sensitizers for radiation at 1151 nm, providing emission bands for LIR calculations (see Fig. 9). Additionally, the researchers co-doped NPs with Er^{3+} ions, which due to the ET from Ho^{3+} ions, were also capable of emission within the 1st biological window. The reported sensitivities were 0.66% °C^{-1} for Ho^{3+}-doped SrF_2 NPs and 0.89% °C^{-1} for Ho^{3+}/Er^{3+}-doped ones. Despite the relatively low sensitivities, the most important is that the authors designed a nanothermometer capable of excitation and emission within BWs and proved that Ho^{3+} ions can provide an important property for biological applications, which is excitation at 1151 nm.

3.3. 1208/1210 nm and 1319 nm excitations *via* Tm^{3+} ions

The laser light at around 1200–1350 nm perfectly matches the 2nd BW, and potentially, it can be used in nanothermometry to excite NPs in biological medium. From the group of Ln^{3+} ions, only Tm^{3+} ions can absorb laser light with the wavelengths mentioned above.[107,108] Through GSA and ESA, followed by CR processes, it is possible to observe the upconversion of Tm^{3+} ions at around 710 and 800 nm.[107,108,114] The spectroscopic properties

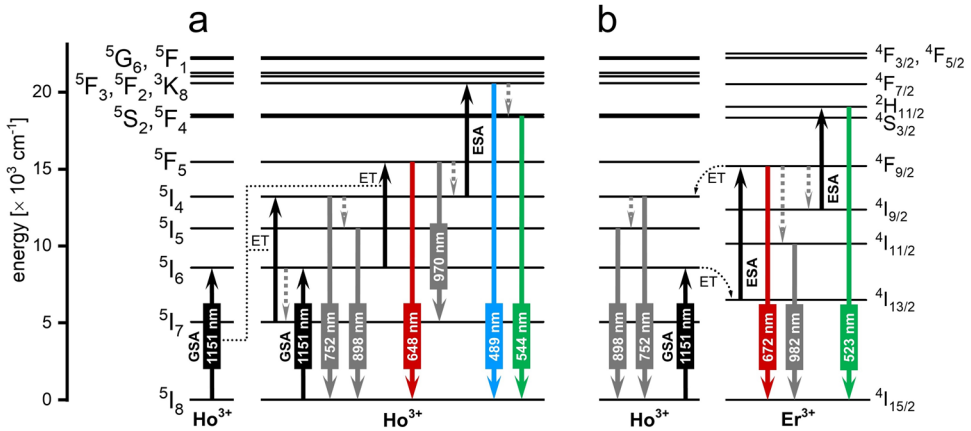

Fig. 9 The mechanism of upconversion in the (a) $NaYF_4$:Ho^{3+}@$NaYF_4$ and (b) $NaYF_4$:Ho^{3+}, Er^{3+}@$NaYF_4$ NPs observed under 1151 nm excitation.[113]

of Tm^{3+} doped into $NaNbO_3$ NPs in the function of temperature were investigated by Pereira *et al.*[60] under excitation with a 1319 nm laser. The researchers revealed that emission with a maximum at around 800 nm, connected with $^3H_4 \rightarrow {}^3H_6$ transition, changed with increasing temperature from 30 to 90 °C (see Fig. 10). After normalization of the emission band at 800 nm, it was possible to distinguish that the broad band is composed of two sub-bands with maxima at around 794 and 807 nm. These emission peaks correspond to two transitions between different Stark sub-levels of Tm^{3+} excited state $^3H_4$. The small energy difference between these sub-levels results in thermal coupling and strong emission intensity dependence on temperature. After deconvolution, it was possible to calculate LIR between 797 and 807 nm at a different temperature, and, as a consequence, the relative sensitivity of the obtained nanothermometer which was around 0.8% $°C^{-1}$ at 30 °C.[60] This untypical system seems to be promising in further investigations based on upconversion of NPs. The same approach was applied by Hernández-Rodriguez *et al.*,[114] who used $YAlO_3$:Tm^{3+} perovskite NPs and 1210 nm as excitation wavelength. In these studies, the researchers also investigated the temperature-depended behaviour of another emission band of Tm^{3+} ions, *i.e.* at around 705 nm related to the $^3F_{2,3} \rightarrow {}^3H_6$ electronic transition. The reported relative sensitivities were 0.26% $°C^{-1}$ at 51 °C, determined from 705/800 nm LIRs and 0.12% $°C^{-1}$ at 26 °C obtained based on 796/802 nm LIRs.[114] Those values are similar to the sensitivities obtained for Nd^{3+}-based nanothermometers; hence, they seem promising for bioapplications.

Grzyb *et al.*[108] studied the Tm^{3+}/Er^{3+}-doped core@shell UCNPs, which present emission from both Tm^{3+} and Er^{3+} ions under 1208 nm excitation with emission bands at 526, 546, 660, 698, 808 and 982 nm. The authors reported that such NPs are capable of high relative sensitivity up to 2.37% $°C^{-1}$ at 57 °C for the 982/698 nm LIR and, most interesting, for the use in bioapplications, 1.69% $°C^{-1}$ at 77 °C and 1.58% $°C^{-1}$ at 67 °C for 660/698 nm and 982/802 LIRs respectively. The maxima of the observed emission peaks fall out of the BW windows; however, the analysed system can be easily adapted to fit the criteria of nanothermometry for bioapplications.

3.4. 1523 nm excitation *via* Er^{3+} ions

Under around 1520–1550 nm laser excitation, only Er^{3+} ions can be exited, resulting in upconversion luminescence or can transfer their energy to different ions.[107] The properties of

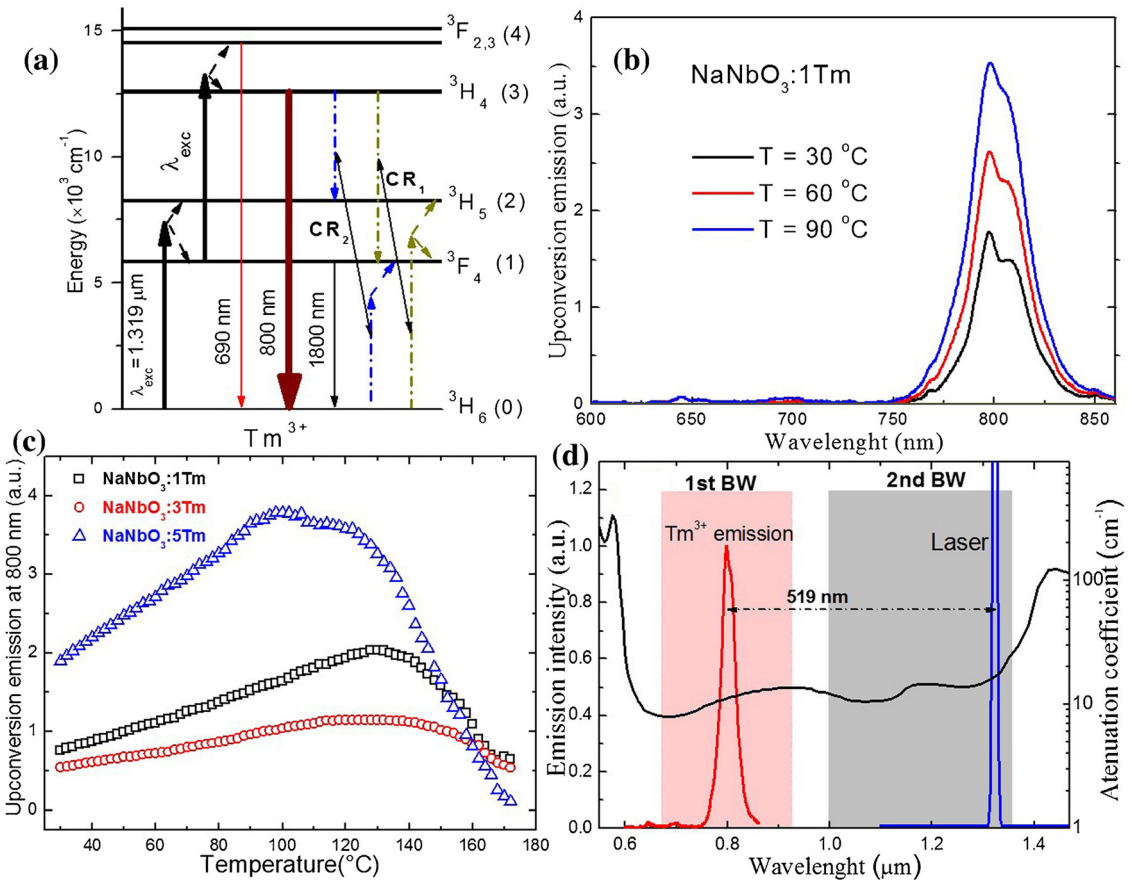

Fig. 10 (a) Simplified energy-level diagram for the excitation and upconversion emission processes in $NaNbO_3$:Tm^{3+} system under pumping at 1319 nm. (b) Upconversion spectra of the sample at 30, 60, and 90 °C. (c) Upconversion integrated area at 800 nm as a function of temperature for three Tm^{3+} concentrations. (d) The emission of $NaNbO_3$:1%Tm^{3+} sample compiled with a 1319 nm laser line along with the attenuation coefficient of human blood (oxygenated) in the 550–1470 nm spectral range. Reprinted from ref. 60, Copyright (2017), with permission from Elsevier.

Er^{3+} ions open the opportunity to use them in nanothermometers excitable within the 3rd BW. Er^{3+} ions undergo excitation *via* GSA/ESA processes and self-sensitization, *i.e.* ET between them, resulting in emission within the 1st BW at around 800 nm, thanks to the $^4I_{9/2} \rightarrow {}^4I_{15/2}$ electronic transition.[115] However, also emission at 970 nm is possible due to the $^4I_{11/2} \rightarrow {}^4I_{15/2}$ transition, which, although it falls outside the range of biological windows, has a broad emission spectrum, and a portion of it falls within the range of the 1st BW, making it usable in nanothermometry. For example, Ryszczyńska *et al.*[115] demonstrated that the LIR of 800 and 970 nm emission bands in SrF_2:Er^{3+} NP observed under 1532 nm excitation can be temperature-sensitive. The researchers achieved a relative sensitivity of around 0.93% $°C^{-1}$ at 100 °C, close to other reports on upconversion NPs. In the presented studies, researchers also investigated the dependence of relative sensitivity on Er^{3+} concentration by analysing NPs doped with 2.1–29% of Er^{3+} ions.[115]

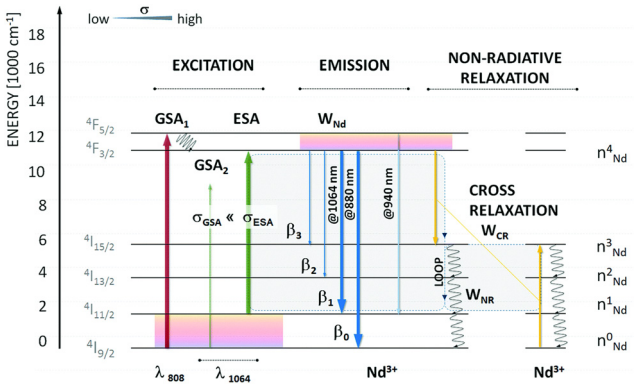

Fig. 11 Energy diagram of Nd^{3+} with possible emission channels upon resonant and non-resonant photoexcitation. The λ = 1064 nm is non-resonant with ground-state absorption. The first excited state, $^4I_{11/2}$, is responsible for the increased absorption cross section at 1064 nm and is thermally coupled with the ground $^4I_{9/2}$ state ($\Delta E(^4I_{9/2} - {}^4I_{11/2}) \sim 2000$ cm^{-1}). Moreover, the $^4I_{11/2}$ state is populated through emission from the metastable $^4F_{3/2}$ level or non-radiative cross-relaxation between two neighbouring Nd^{3+} activators. The loop, which doubles the $^4I_{11/2}$ population, is schematically shown (grey rectangles). Used with permission of The Royal Society of Chemistry, from ref. 117; permission conveyed through Copyright Clearance Center, Inc.

4. Systems based on simultaneous down-shifting and upconversion

In some of the systems found in the literature, the researchers used the possibility of obtaining both upconversion (anti-Stokes) and down-shifted (Stokes) emission to develop nanothermometers with the possibility of use in bioapplications. The Marciniak's group specializes in this approach and has published all these reports.[70,117–119]

The typical upconversion phenomenon under 1064 nm excitation is relatively rare as there are no Ln^{3+} ions which can be excited by this wavelength *via* a resonant GSA process. However, under 1064 nm laser radiation, it is possible to excite Ln^{3+} ions *via* a non-resonant process,[120] which may result in photon avalanche (PA) in some cases.[35,121,122] The PA process relies on the non-resonant excitation followed by the resonant ESA and a loop of CR processes. The scheme of energy processes taking place in such systems is presented in Fig. 11. The temperature of the avalanching system may influence the effectiveness of the PA process. Marciniak *et al.*[117] investigated the dependence of Nd^{3+} emission at 880 nm in various hosts (see Table 3) on temperature under non-resonant 1064 nm excitation by applying an avalanche-like

Table 3 Nanothermometers using simultaneously down-shifted and upconverted luminescence

Type of nanoparticles	Emitter	Excitation (nm)	Emission bands for temperature sensing (nm)	Reported max. sensitivity	Reported temperature range (°C)	Technique	Comments	Ref.
$NaYF_4$:Nd^{3+}	Nd^{3+}	808	LIR = (720–740)/(870–900)	1.1% $°C^{-1}$ at 137 °C; ΔT = ~2 °C at RT	−190 to 150	LIR	Studies show how the Nd^{3+} concentration influences thermometers' performance	70
Y_2O_3:Nd^{3+}, Gd_2O_3:Nd^{3+}, $YGdO_3$:Nd^{3+}, $YAlO_3$:Nd^{3+}, $Y_3Al_5O_{12}$:Nd^{3+}, $LiLaP_4O_{12}$:Nd^{3+}	Nd^{3+}	1064 + 808	LIR = 880 (1064 nm exc.)/880 (808 nm exc.)	2–5% $°C^{-1}$	0–300	LIR	The photon avalanche process was applied for temperature sensing	117
$LaPO_4$:Nd^{3+}	Nd^{3+}	1060 + 808	LIR_1 = 890 (1060 nm exc.)/890 (808 nm exc.); LIR_2 = 810 (1060 nm exc.)/890 (808 nm exc.); LIR_3 = 750 (1060 nm exc.)/890 (808 nm exc.)	S_1 = 7.19% $°C^{-1}$ at 30 °C; S_2 = 3.04% $°C^{-1}$ at 100 °C; S_3 = 4.35/°C at 180 °C	0–300	LIR	The researchers used an alternative method for LIR determination, *i.e.* using two laser lines, 808 and 1064 nm, to excite Nd^{3+} ions at different temperature	118
$NaYF_4$:Nd^{3+}	Nd^{3+}	1060 nm + 808 nm	LIR = 880 nm (1060 nm exc.)/880 nm (793 nm exc.)	5% $°C^{-1}$ at 0 °C (max. 19.1% $°C^{-1}$ at −73 °C); ΔT = 0.1–0.2 °C	−73 to 200 °C	LIR	The article reports the effects of the NPs size (fife sized in the 20–200 nm) on the sensitivity of nanothermometers	119

process. The researchers developed a new approach to temperature sensing by determining how the ratio between emission obtained *via* resonant (808 nm) and non-resonant (1064 nm) excitations changes with temperature. The relative sensitivities obtained by this approach are one of the highest reported, between 2 and 5% $^{\circ}C^{-1}$, depending on the used host. The PA process results in high emission intensity, usually higher than can be expected from UCNPs.[117] However, PA requires high-power densities of excitation, usually in the range of kW cm^{-2}.[122] Therefore, the proposed way of temperature sensing seems challenging for bioapplications.

In another two studies published by Trejgis *et al.*[118,119] the temperature-dependent emissions of $LaPO_4$:Nd^{3+} NPs and $NaYF_4$:Nd^{3+} were measured under similar to the conditions mentioned above, *i.e.* the researchers used 808 and 1060 nm excitations. In the case of the $LaPO_4$:Nd^{3+} NPs, three LIRs were determined using the fact that the emission at 890 nm related to the $^4F_{3/2} \rightarrow {}^4I_{9/2}$ transition of Nd^{3+} ions shows different dependence of intensity on temperature when samples are excited with 808 and 1060 nm. The other two LIRs were based on the intensity ratio of the emission at 750 nm ($^4F_{7/2}$,$^2S_{3/2} \rightarrow {}^4I_{9/2}$) or 810 nm ($^4F_{5/2}$,$^2H_{9/2} \rightarrow {}^4I_{9/2}$) obtained by non-resonant excitation to the emission at 890 nm ($^4F_{3/2} \rightarrow {}^4I_{9/2}$) obtained by resonant excitation with an 808 nm laser. The thermometric properties of the other type of NPs, *i.e.* $NaYF_4$:Nd^{3+}, were determined by measuring emission at 880 nm under two excitation lines (808 and 1060 nm). That approach led to enormous values of relative sensitivity, like for the Ln^{3+}-based nanothermometers, which reached up to 7.19% $^{\circ}C^{-1}$ for $LaPO_4$:Nd^{3+} NPs and 5% $^{\circ}C^{-1}$ for the $NaYF_4$:Nd^{3+} in the physiological temperature range.

Another example of nanothermometers utilizing Stokes and anti-Stokes emission are $NaYF_4$:Nd^{3+} NPs, which under 808 nm excitation present an emission band in the 700–750 nm range related to $^4F_{7/2}$,$^4S_{3/2} \rightarrow {}^4I_{9/2}$ transition of Nd^{3+} ions and a broad down-shifted emission band in the 850–950 nm range related to $^4F_{3/2} \rightarrow {}^4I_{9/2}$ transition of Nd^{3+} ions.[70] The approach presented by Maciejewska *et al.*[70] differs from the rest of the above-mentioned articles, *i.e.* the researchers used single beam excitation. However, the LIR between these bands is still temperature-sensitive, allowing for relatively high sensitivity like for the Nd^{3+}-based thermometers, *i.e.*, 1.1/°C at 137 °C.

In summary, the use of two types of emission for developing a nanothermometer undoubtedly results in significantly higher sensitivity compared to other known methods. Although applying two different excitation wavelengths poses some difficulties in real applications, the high relative sensitivity values may compensate for these challenges. Unfortunately, there are no reports on the practical applications of such nanothermometers in *ex vivo*, in vivo, or *in vitro* research.

5. Host nanomaterials for Ln^{3+} ions for temperature sensing in the biological windows range

Over the years, many luminescent materials were tested as potential nanothermometers, such as polymers, nanogels, nanodiamonds, organic–inorganic hybrids, organic dyes, quantum dots, carbon dots, and Ln^{3+}-doped UC inorganic nanomaterials.[123] Ln^{3+}-doped NPs are also suitable for real-time temperature monitoring in the biomedical field.[102] They form a distinct class of optical materials designed to produce emission lines when excited by NIR light without photobleaching, autofluorescence, and phototoxicity.[123] Inorganic materials, in most cases, are transparent to the NIR excitation light, and they are usually doped with appropriate Ln^{3+} ions in optimized concentrations, giving them exceptional properties.[124] In many studies, an activator ion (emitter) is often embedded in a host material and a luminescence sensitizer ion, facilitating the transfer of the absorbed energy. However, our review also covers instances where luminescence can be observed using only one type of Ln^{3+} ion (playing a role as both activator and sensitizer) incorporated into the host.[80]

The temperature sensitivity of Ln^{3+}-doped NPs is often associated with changes in their optical properties in response to temperature variations. Therefore, the selection of host matrix composition, crystallographic structure, size of NPs, dopant type, and concentration is crucial in luminescence nanothermometry.[44,117] Jia *et al.*[125] proved that temperature sensitivity decreases with increased phonon energy of the host material due to the possibility of multi-phonon quenching. Therefore, it is important to note that thermal sensitivity can vary across different systems and depends on the extent of thermally induced spectral variations, *i.e.* temperature variations that can lead to changes in the crystal lattice, which impact Ln^{3+} energy levels and their emission properties. Additionally, the host material can influence the efficiency of the ET between the matrix and the dopant ions. Because of this, choosing a host that will not quench NPs emissions is extremely important. Understanding and manipulating these factors allow researchers to design Ln^{3+}-doped NPs with tailored temperature sensitivity for various optical temperature sensing applications.[86,117,126]

In this review article, we have collected materials reported for remote temperature-sensing applications in the range of biological windows. We have divided these materials into several major groups based on the host matrix compositions, *i.e.* oxides, fluorides, phosphates, and vanadates. These Ln^{3+}-doped materials hold great promise for optical nanothermometry due to their narrowband absorption and emission characteristics, ratiometric and luminescence lifetime temperature sensing capabilities, excellent photostability, low cytotoxicity, and ease of biofunctionalization.[44,126]

5.1. Oxides

5.1.1. Rare earth oxides. Rare earth oxides (RE_2O_3) NPs are among the most extensively studied materials for generating white light.[127] Most RE_2O_3 NPs have the advantage of being chemically stable in water without dissolving.[86] This property allows for use them in bioimaging, therapy, and temperature sensing.[91,128] The most important methods for synthesizing RE_2O_3 NPs are the precipitation and the combined Pechini-foaming methods. However, in both cases, the product must be calcinated at high temperature values to eliminate organic components and support crystallization.[90,91,93]

Among all RE_2O_3, yttrium oxide (Y_2O_3) is the most popular host for luminescent Ln^{3+} ions and ceramic material in phosphor technology, mainly due to its low-cost and well-match ionic radius (Y^{3+}) to most Ln^{3+} ions. Furthermore, this compound has a broad transparency range (0.2–8 μm) with a band gap of 5.6 eV. Its high chemical stability, thermal conductivity (at 293 K is 8–12 $W\,m^{-1}\,K^{-1}$), refractive index and melting point (2451 °C), as well as low phonon energy (600 cm^{-1}),[129] and cytotoxicity, have made Y_2O_3 a suitable choice as host for Ln^{3+} ions in nanothermometry.[44,93,103,117,128]

Lanthanum, gadolinium, and lutetium oxides (La_2O_3, Gd_2O_3, and Lu_2O_3) are also often used as hosts for Ln^{3+}. These compounds are characterized by higher phonon energies than Y_2O_3 (~400 cm^{-1}, ~600 cm^{-1} and ~620 cm^{-1} for La_2O_3, Gd_2O_3 and Lu_2O_3 respectively).[72,90,103,117,130] In the case of Gd_2O_3, the properties of the crystal lattice result in lower sensitivity.[72,123] Savchuk *et al.*[66] used Lu_2O_3 as a host material, but in this case, relative temperature sensitivity was also lower than that of the nanothermometer based on fluoride discussed in this article (see Table 1).

5.1.2. Other oxides. Silva *et al.*[87] used titanium dioxide (TiO_2) as a host material for Ln^{3+} dopant ions. TiO_2 NPs exhibit high photodegradation efficiency, notable photocatalytic activity, remarkable stability, and they are chemically inert, thanks to which they are often used in biology. However, the synthesis process of this compound is difficult due to the significant mismatch in ionic radii between the Ti^{4+} and RE^{3+} and the charge imbalance. Moreover, thermal annealing at high temperature values after synthesis (post-treatment) is required. The impact of annealing temperature on TiO_2 luminescence properties reveals an enhancement in the crystallinity degree and the formation of the brookite phase, which exhibits the highest luminescence.[87] For this reason, this compound is used relatively rarely as a nanothermometer compared to RE_2O_3.

5.2. Oxychlorides

Another host less commonly used in nanothermometry in the range of biological windows is lanthanum oxychloride (LaOCl). This compound is promising for use in nanothermometry because of its versatility to host various RE ions. It is worth mentioning that this material's lattice phonon energy (~430 cm^{-1}) is one of the lowest and similar to fluoride hosts, reducing the probability of non-radiative multi-phonon relaxation. Furthermore, the crystal field splitting of the thermalized $^4I_{11/2}$ energy state of Nd^{3+} ions is more visible in the LaOCl system, which is an advantage in luminescence ratiometric nanothermometers. LaOCl NPs are also relatively easy to synthesise. Renero-Lecuna *et al.*[89] obtained this compound at low temperature, which resulted in monodispersed and ultra-small crystals. However, additional surface modification was necessary to make these particles hydrophilic.

5.3. Tungstate compounds

Another group of compounds considered to be excellent hosts for Ln^{3+} ions because of their high thermal and chemical stability are monoclinic tungstates, mainly potassium gadolinium/lutetium double tungstates, $KGd(WO_4)_2$ and $KLu(WO_4)_2$.[66,67,74] This group of materials provides large values of absorption and emission cross-sections for Ln^{3+} ions with negligible luminescence quenching, which are essential for optical nanothermometry. To synthesise the compounds mentioned above, the Pechini sol–gel method, followed by calcination at high temperatures, gives the intended monoclinic structure—unfortunately, the synthesis results in agglomerated NPs. Savchuk *et al.*[67] obtained non-defined shapes of NPs of sizes ranging from 2 μm to 6 μm with smaller NPs (70–150 nm). Whereas Nexha *et al.*[74] synthesized nanocrystals with sizes up to 1.8 μm and irregular shapes. The large size of crystals obtained may be a barrier to biomedical applications.

5.4. Materials with perovskite structure

Among the Ln^{3+}-doped nanomaterials, perovskite oxides emerge as promising host candidates for optical temperature sensors thanks to their favourable mechanical and thermal properties and chemical stability.[60,114,117] Especially interesting as a host material for Ln^{3+} ions is yttrium *ortho*-aluminate nanoperovskite ($YAlO_3$). Hernández-Rodríguez *et al*. obtained this compound using the Pechini citrate sol–gel method, followed by annealing at high temperatures.[114] The synthesized crystals were homogeneous and nanosized. Another host compound from this group is sodium niobate ($NaNbO_4$), which is characterized by low density, as well as by the presence of photo-refractive and photo-catalysis effects. Pereira *et al.* synthesized Ln^{3+}-doped $NaNbO_4$ crystals using the Pechini sol–gel method. After heat treatment, the NPs were about 70 nm in size and had high colloidal stability.[60] Therefore, the perovskite oxides are excellent nanoprobes for potential use as optical nanoheaters in the BW range.

5.5. Garnet nanostructures

Nowadays, yttrium aluminium garnet (YAG; $Y_3Al_5O_{12}$) doped with Ln^{3+} ions, especially Nd^{3+}, has been extensively utilized in solid-state laser technology. Consequently, its optical properties have been thoroughly investigated and documented. Moreover, YAG is a popular host material for Ln^{3+}-doped NPs, especially in thermal sensitivity.[69,82,85,86,117,123,125] YAG is known for its excellent thermal stability due to resistance to high temperatures, such as 1200 °C without phase changes and degradation.[131] The good thermal conductivity of this material allows for efficient heat transfer and, thus, uniform temperature distribution within NP and lack of localized heating. Moreover, YAG is chemically inert, which provides chemical stability and prevents chemical reactions with surrounding molecules. Its transparency in the infrared region is advantageous for applications where the emission or absorption of NIR is important. Therefore, the combination of YAG's thermal stability and optical transparency with the luminescence properties of Ln^{3+} ions make it a suitable choice for various temperature sensing and thermal imaging applications. Moreover, it has been proven that using nanogarnet as a host ensures narrower emission lines than widely reported fluoride hosts. Preparation of a garnet structure at the nanoscale with sufficient crystalline quality for optical applications has been proven. Cantarano *et al.*[69] presented the solvothermal synthesis of the stable colloidal suspension of YAG in ethanol. Unfortunately, this synthesis required the material's surface modification to apply it in biomedicine. Benayas *et al.*[85] proposed the combustion synthesis of YAG, which includes the bulk-to-nano transition. Intensely exothermic reactions between metal nitrates

and organic fuel, reaching temperature values above 1500 °C, generate a foamy product with nano-sized crystallites.

Similar properties to YAG has gadolinium scandium aluminium nanogarnet (GSAG; $Gd_3Sc_2Al_3O_{12}$). Only a single article was published using this host material as a temperature sensor in the BW range.[86] Dantelle *et al.*[86] reported the GSAG synthesis, based on a solvothermal method at a high temperature (350 °C), necessary to obtain the desired crystallinity, morphology, and nanometric size. It has been proved that using higher temperatures during the synthesis process provides increased energy for the NPs' growth and contributes to the expansion of crystalline domains. However, obtaining the pure crystal structure of GSAG requires supplying more energy during the synthesis than for YAG. Notably, the overwhelming advantage of the GSAG over YAG is the presence of Gd^{3+} ions in its structure, which enables the potential use of these nanosystems as MRI contrast agents.

Another compound belonging to the nanogarnet group is yttrium gallate (YGG; $Y_3Ga_5O_{12}$), synthesized by the citrate sol–gel method.[77] YGG is less commonly used in nanothermometry than the YAG mentioned above. However, it is worth noting that YGG exhibits low cytotoxicity and does not require any functionalization to enter the cell.

Summing up this part, garnet-type nanostructures demonstrate high transparency across the UV to mid-IR range, excellent chemical stability, high thermal conductivity, and high-energy phonons for efficient heat generation.[69,82,86,125,132] They are widely used as hosts for Ln^{3+} ions, generating emissions with high quantum yields and demanded properties for nanothermometry applications.

5.6. Silicates

Chen *et al.*[76] proved that Ln^{3+}-doped bismuth silicate (Bi_2SiO_5) inorganic NPs, characterized by uniform size and morphology, show significant potential as luminescent ratiometric nanothermometers for precise temperature sensing. Bi_2SiO_5 is a promising phosphor host for Ln^{3+} ions owing to its attractive properties such as low cost, low toxicity, excellent chemical stability, and good lattice matching with Ln^{3+} ions. However, the hydrothermal synthesis of the uniform structure requires an additional post-treatment step based on the silica coating of the as-prepared nanocrystals. The presence of the SiO_2 layer allows compound calcination at high temperatures without matrix degradation. The appropriate annealing temperature increases the host crystallization and provides good dispersion of Ln^{3+} ions inside the lattice. Despite its advantages, the described compound is not popular in BW nanothermometry.

5.7. Borates

The beta-barium borate (β-BaB_2O_4) crystals serve as excellent host matrices for Ln^{3+}. During the synthesis, Ba^{2+} ions can be easily replaced by Ln^{3+} in borate crystals without significant crystal deformation. These NPs can be prepared using the polymeric precursor method and crystallized after a heat treatment.[88] β-BaB_2O_4 are characterized by high stability and a broad NIR transparency window (from 190 nm to 3300 nm). Moreover, this compound is of significant interest because of its nonlinear optical properties characterized by high second harmonic generation efficiency. Ferreira *et al.*[88] applied β-BaB_2O_4 as a host for Ln^{3+} ions and widely studied the obtained NPs for optical nanothermometry purposes.

5.8. Phosphates

Phosphate-based nanomaterials can be attractive host matrixes due to easy synthesis and biofunctionalization, allowing NPs' biocompatibility and low toxicity.[92] The most common synthesis method of phosphates is co-precipitation. The crystals obtained are nanosized and create stable water colloids.[57,84,92] In these host materials, optically active ions are well-separated because of the properties of the crystal lattice, preventing in the same way significant cross-relaxations and luminescence quenching. Most studies focus on Ln^{3+}-doped orthophosphates of general formula $LnPO_4$ as they usually provide higher sensitivities than post-transition metals analogues.[92,118] This structure shows high physicochemical stability and resistance in various media. From the many types of phosphates, those based on the metal from the lanthanides series instead of the post-transition metals show higher sensitivities.[123] Nevertheless, a larger distance between activator ions is found in tetraphosphates such as $LiLaP_4O_{12}$, $KLaP_4O_{12}$, $NaLaP_4O_{12}$, and $LiNdP_4O_{12}$, which makes those matrices promising to develop more efficient phosphors.[57,84,117] The significant influence of the alkali ion size on the distance between the alkali and emitting ion is responsible for this phenomenon. Consequently, the $LiLaP_4O_{12}$ compound attains the highest values of relative sensitivities.[84,117]

5.9. Vanadates

Many articles report the vanadate matrix used as a host for Ln^{3+} ions to get nanothermometers working in the BW range. Vanadates can offer good chemical stability, low phonon energy, excellent electro-optical properties, and compatibility with other materials, making them suitable for various environments and potential applications, including biological and medical contexts.

Thanks to its distinctive mechanical and optical properties, yttrium orthovanadate (YVO_4) is the most commonly used. The key advantages of the Ln^{3+}-doped YVO_4 nanothermometers include the simplicity of synthesis, the oxide host stability, high absorption cross-section at 808 nm (making it an ideal host for Nd^{3+}), and the potential to operate in biological windows. This compound can be prepared using the Pechini method and calcination to obtain a crystalline structure.[56,64,125,133]

Ln^{3+}-doped lutetium orthovanadate ($LuVO_4$) is another representative rare-earth vanadate. Those NPs can be obtained using the hydrothermal method. Like YVO_4, $LuVO_4$ NPs need the calcination process to achieve crystallinity and high UC intensity. Xiang *et al.*[104] proved that, in some cases, $LuVO_4$ allows a higher relative sensitivity than YVO_4. However, to obtain such a result, it was necessary to cover these NPs with a layer of silica.[104,134]

Gschwend *et al.*[71] chose a vanadate structure based on bismuth vanadate ($BiVO_4$) because it was reported as an excellent host for Nd^{3+} ions, facilitating deep penetration (3–20 mm) observed in chicken tissue and bovine liver.[71,135] The authors obtained $BiVO_4$ crystals by flame spray pyrolysis, proving high

crystal purity. Moreover, after analysing the energy diagram for Nd^{3+} in monoclinic $BiVO_4$, the researchers concluded that the peaks in the emission spectrum align well with the calculated radiative decays, which results in effective Nd^{3+} excitation.[71] Unfortunately, the vanadate-based particles are often not homogeneous (the presence of agglomerates), which may hinder the potential application in biomedicine.

5.10. Fluorides

Due to their excellent anti-Stokes luminescence properties associated with the low-phonon energy (below 500 cm^{-1}), simple strategies for the control of NPs size/shape/morphology/spectral tuning, and surface biofunctionalization, fluorides dominate almost all luminescent inorganic hosts used in nanothermometry.[86,103,115,136]

Sodium rare-earth tetrafluorides ($NaREF_4$; RE = Y, Er, Nd, Gd, Yb) are the most commonly used host materials in nanothermometry.[55,66,70,73,79,80,94,97–99,102,113,119] $NaYF_4$ is one of the most efficient matrices for Ln^{3+} luminescence due to easy size control of NPs, surface chemistry adjustment, and its low lattice phonon energy ($\sim$350–500 cm^{-1}), which helps minimize multiphonon non-radiative processes of excited states.[137,138] Two known polymorphs of the $NaYF_4$ structure are the crystallographic α-cubic and β-hexagonal phases.[119] However, tetrafluorides that crystallize into a β-polymorph are more suitable for ratiometric thermometry applications because the symmetry of Ln^{3+} ions in hexagonal β-polymorph favours higher probabilities of radiative transitions, and as a consequence, much more efficient luminescence.[66,70,97,102,113,119] Additionally, $NaREF_4$ NPs are usually obtained using the thermal decomposition method of synthesis (or precipitation in high-boiling solvents), which has many advantages.[94,97,98,102,113,119,139,140] This method yields high quality with a pure crystal phase, excellent uniformity in size and shape, strong UC emission, and a large product volume.[141] Unfortunately, a significant disadvantage of this method is the need to modify the NPs' surface, which are hydrophobic directly after synthesis.[141,142]

Many researchers selected a lithium RE tetrafluoride ($LiREF_4$) host based on its low phonon energies (200–490 cm^{-1}), relatively high crystal field strength, size-tuneable properties, and the potential for further development into multifunctional core@shell nanostructures.[59,81,101,105,136] Moreover, the advantage of $LiREF_4$ NPs over $NaREF_4$ is that it enables the spectral resolution of the fine Stark structure of the Nd^{3+} $^4F_{3/2} \rightarrow {}^4I_{11/2}$ transition, making it feasible for implementing photoluminescence temperature sensing.[59] $LiREF_4$ are usually synthesized by the thermal decomposition method, with the abovementioned advantages.[59,81,101] Khadiev *et al.*[136] used a tetragonal host based on $LiYF_4$ because this material provides efficient substitution of Y^{3+} ions by Ln^{3+} ions without valence change and charge imbalance. Such an approach opens up the possibility of achieving high concentrations of Ln^{3+} in structure with limited luminescence concentration quenching. Hazra *et al.*[101] studied $LiErF_4$@$LiYF_4$ as single-band nanothermometers, which stemmed from the necessity to address inhomogeneous light attenuation by tissues. This property is crucial for advancing thermal mapping to achieve the highest contrast possible, mainly provided by the broad emission band located in the 3rd BW. Another important host based on $LiREF_4$ structure is $LiLuF_4$. Nd^{3+}-doped $LiLuF_4$ was studied by Skripka *et al.*[59] and Huang *et al.*[81] due to its sensitive NIR-to-NIR luminescence for subtissue bioimaging.

A relatively commonly used host compound for Ln^{3+} ions is lanthanum trifluoride (LaF_3).[41,61,65,78,83,95] In addition to all the properties typical for fluorides, it is characterized by an easy synthesis method based on wet chemistry. LaF_3 annealing is needed immediately after synthesis, but this does not negatively affect its crystallinity and size. Rocha *et al.*[78] experimentally proved that Ln^{3+}-doped LaF_3 NPs undergo moderate size enlargement when subjected to thermal annealing at 500 °C (in the ambient atmosphere), notable lattice ordering, and removal of defects through recombination. Due to the structural changes induced by temperature, NPs exhibited a significant increase in luminescence brightness and a noticeable reduction in emission linewidth. The simultaneous brightness and thermal sensitivity improvement would lead to enhanced thermal resolution achievable during sub-tissue photothermal therapies based on this compound. Notably, the LaF_3 host shows low toxicity and high biocompatibility, which have been proved in numerous *in vivo* and *in vitro* experiments.[61,65,83,95]

Other host compounds from the fluoride group are alkali earth fluorides, such as CaF_2 and strontium fluoride (SrF_2), with low phonon energy (for CaF_2 $\sim$ 470 cm^{-1} and SrF_2 $\sim$ 290 cm^{-1}) that reduce the probability of non-radiative relaxing processes of dopant ions.[58,68,75,115] Those compounds have good optical properties and high thermal conductivity; they are biocompatible and thermally stable and can be obtained in nanometric size.[123] Ryszczyńska *et al.*[115] synthesized Ln^{3+}-doped SrF_2 crystals smaller than 18 nm, while Quintanilla *et al.*[58,68] and Soares *et al.*[75] obtained Ln^{3+}-doped CaF_2 nanomaterials smaller than 21 nm. The use of the hydrothermal method ensured high NPs stability in aqueous solution. Notably, the synthesis route chosen by the authors is characterized by simplicity and high adaptability, which makes these compounds more attractive in potential applications.

Cubic barium lanthanum fluoride (Ba_2LuF_7) is another example of a host with properties demanded for nanothermometry. Li *et al.*[96] prepared Ba_2LuF_7 doped with Ln^{3+} ions as nanomaterial using synthesis in high-boiling-point solvents.

5.11. Core@shell and core@multishell structures

Here, we emphasize strategies for developing highly sensitive nanothermometers by highlighting the role played by the morphology of the host in which Ln^{3+} ions are incorporated. This involves taking into account structures such as core@shell or multishelled configurations.[95,101]

The purpose of adding the inert layer onto the active core is to protect it from possible oxidation-related heat damage. Furthermore, due to the inert shell's ability to prevent the active ions on the NPs' surface from relaxing non-radiatively, the emission intensity of the core@shell nanocrystals is enhanced.[123] Examples of core@shell structures that can be used in temperature sensing within the BW ranges are LaOCl:Nd^{3+}@LaOCl,[89] Ba_2LuF_7:Yb^{3+},Nd^{3+}, Er^{3+}@Ba_2LaF_7,[96] $NaYF_4$:Tm^{3+},Er^{3+}@$NaYF_4$,[108] $LiLuF_4$:Nd^{3+}@$LiLuF_4$,[59] $LiErF_4$@$LiYF_4$,[101] $LiYbF_4$:Er^{3+},Ce^{3+}@$LiYF_4$,[105] $NaNdF_4$@$NaYF_4$,[80]

$NaYF_4:Nd^{3+}$@$NaYF_4$,[80] $NaNdF_4$@$NaGdF_4$,[143] and $NaYF_4:Ho^{3+}$, Er^{3+}@$NaYF_4$.[113]

The active core@active-shell and core@multishell structures allow flexibility in design and easy integration of dopants with the required spatial distribution like in $NaGdF_4:Yb^{3+},Tm^{3+}$@$NaYF_4:Yb^{3+}$@$NaGdF_4:Yb^{3+},Nd^{3+}$@$NaGdF_4$[73] and $NaYF_4:Yb^{3+},Ho^{3+}$@$NaYF_4:Yb^{3+},Er^{3+}$@$NaNdF_4:Yb^{3+}$[94] nanomaterials. This enables the manipulation of ET processes between various ions in different layers. For example, Wei *et al.*[97] used in the study an active-core@active-shell $NaYbF_4:Nd^{3+}$@$NaYF_4:Nd^{3+}$ nanostructure to raise the concentrations of Yb^{3+} and Nd^{3+} ions while reducing unwanted cross-relaxation. Ximendes *et al.*[41,95] proposed surrounding the Yb^{3+}-doped LaF_3 core with heavily Nd^{3+}-doped LaF_3 as a heating unit.

Another interesting idea was demonstrated by Marciniak's group that synthesized pure $NaNdF_4$ nanocrystal cores coated by additional secondary shells, $NaYF_4$ as a spacer and $NaYF_4:Nd^{3+}$ as a temperature-sensitive layer.[80] The parasitic cross-relaxation processes have been significantly decreased by spatially separating the heating part ($NaNdF_4$) from the luminescence and sensing part ($NaYF_4:Nd^{3+}$) by adding an inactive spacer shell. It provided sensitive temperature measurement upon NIR excitation and efficient emission within the spectral range of BWs.

Another example of core@multishell structure host nanomaterial is $NaYF_4$@$NaYF_4:Yb^{3+},Nd^{3+}$@CaF_2.[99,100] The reasons behind using CaF_2 as the outer layer were significant transparency in a wide spectral range (0.13–10 μm), good lattice match with the core material, good chemical stability, and biocompatibility.

In conclusion, core@shell and core@multishell nanoarchitecture notably improve temperature-sensing capabilities and increase the brightness of emissions.[100,105] Nonetheless, whether viewed from a synthetic or spectroscopic perspective, these structures comprise highly complicated systems. Furthermore, most are hydrophobic due to their organic surface coatings; hence, additional surface modifications are required for biomedical applications to make them water-dispersible.[41,144]

6. Biological studies and bioapplications of nanothermometers

Using Ln^{3+}-doped NPs is generally non-invasive when compared to other temperature sensing techniques. Their nanoscale size makes delivering to various targeted organelles, cells, tissues, and organs easier.[117,126] Ln^{3+}-doped nanomaterials can be exited and present emission within the range of BWs, which reduces their interactions with biological tissue, absorption and scattering light.

Many articles extensively discuss the potential applications of nanothermometers. However, there are relatively few papers that present their real applications. We collected these articles in this review and presented their most significant achievements.

6.1. *In vivo* experiments

Tissue scattering and absorption are crucial factors *in vivo* experiments. In addition to the optical losses of the excitation light beam (decreasing on-target laser power density) resulting in deteriorated emission of NPs, its absorption may significantly affect the obtained results because the absorbed light is converted into another form of energy, most frequently into heat, raising the local temperature.[126] Unfortunately, it has been reported that system inhomogeneities, detection system limitations, interference with contaminants, and unexpected dependence on the system's response under experimental conditions can all cause artefacts during *in vivo* experiments and bias the temperature readouts.[61] Hence, for the optimized application in tumour hyperthermia, the *in vivo* models should ideally involve the intravenous administration of luminescent nanomaterials or their direct injection into the organ of interest. On the contrary, subcutaneous or intradermal injections may be more suitable in studies where minimal tissue interference and controlled NPs concentrations are essential.

Ximendes *et al.*[95] checked the ability of injected core@shell $LaF_3:Nd^{3+}$@$LaF_3:Yb^{3+}$ NPs to reveal fundamental tissue properties *in vivo* conditions by monitoring subcutaneous thermal relaxation. Small changes in subcutaneous tissue relaxation times could be used to identify possible changes in the tissue's density, specific heat, thermal diffusivity and thermal conductivity. These alterations could be associated with the presence of conditions such as cancer, tumours and other diseases. The scientific group used a simple *in vivo* experiment based on subcutaneously injected NPs into an anaesthetized mouse (Fig. 12). Safe heating was accomplished by setting the 808 nm laser beam's power density to 0.7 W cm^{-2} and extending the thermal treatment to four minutes. The mouse's surface temperature rose from 34.2 to 40.5 °C under these irradiation conditions without endangering its skin. The researchers used a low-power 790 nm, 30 mW laser diode to record the NPs' luminescence at 1060 nm. The validity of using $LaF_3:Nd^{3+}$@$LaF_3:Yb^{3+}$ NPs as precise and dependable subcutaneous thermal sensors for *in vivo* applications is supported by the excellent agreement between the values obtained by subcutaneous luminescence nanothermometry for both tissue absorption coefficient and tissue thermal diffusivity with those previously reported in the literature.[95] The same scientific group showed the capability of $LaF_3:Yb^{3+},Nd^{3+}$@LaF_3 NPs for real-time subcutaneous measurements in chicken breast.[41]

Another research group presented a novel approach to temperature sensing in living organisms, namely the Ln^{3+}-doped $NaGdF_4:Yb^{3+},Tm^{3+}$@$NaYF_4:Yb^{3+}$@$NaGdF_4:Yb^{3+},Nd^{3+}$@$NaGdF_4$ core@multishell nanocomposite that emits light in the 2nd and 3rd BW.[73] Hu *et al.* proved the lack of toxicity of those NPs in the mouse based on the analysis of her main organs. The NPs' temperature imaging revealed that the average temperature of the right mouse paw was elevated to 39.6 °C, while the average temperature of the left paw was 37.1 °C. These findings demonstrated the NP's capacity to detect and visualize body temperature in a living organism for disease diagnosis and physiological process monitoring.

Carrasco *et al.*[83] decided to check the application possibility of Nd^{3+}-doped LaF_3. These NPs can perform intratumoral thermal sensing, fluorescent tumour localization, and *in vivo* photothermal heating due to the unique optical properties of

Nd^{3+} ions at high doping concentrations. They induced the growth of subcutaneous tumours in athymic nude mice and began photothermal therapy using NPs injected into the tumours. The photothermal therapy was completed using an 808 nm laser and proved to be effective. Notably, they monitored the intra-tumoral temperature by analysing NPs spectral properties. In turn, the optimized ternary domain $NaYF_4$@$NaYF_4$:Yb^{3+},Nd^{3+}@CaF_2 NPs were thermographically mapped to determine temperature distribution using a living mouse by Tan *et al.*[99]

Shen *et al.*[61] demonstrated a hyperspectral imaging system in a small animal model using 808-nm excitable NPs and their emission ranging from 900 to 1700 nm. They observed that the relative intensities of the Tm^{3+} emission bands, which are also utilized for ratiometric thermal sensing and are centred at 1230 and 1470 nm, are significantly reduced due to skin absorption. Because of the difficulties encountered with the multiple uncontrollable factors (vascular blood flow and aggregation of NPs), they decided to perform *ex vivo* experiments on the cortex tissues. They concluded that tissue-induced optical distortions significantly impact ratiometric thermal sensing, considered the most dependable method for remote thermal sensing.[61]

The above-presented findings show the great potential of NIR-emitting nanothermometers for heat transfer research, non-invasive subcutaneous anomaly detection, and diagnostic applications in small animals.

6.2. *In vitro* experiments

Experiments carried out outside a living organism, usually in a controlled setting like a laboratory, are referred to as *in vitro* experiments. These experiments provide a controlled and standardized environment, allowing researchers to manipulate variables precisely. Moreover, they offer several advantages, such as ethical considerations and reproducibility. Unfortunately, they also have limitations related to biological relevance and difficulties in extrapolation to *in vivo* conditions.

Quintanilla *et al.*[68] obtained a hybrid nanostructure based on plasmonic gold NPs (optical heater) and luminescent CaF_2:Nd^{3+},Y^{3+} NPs (nanothermometer). Both materials can be excited at the same wavelength (808 nm) within the 1st BW, while the emission of the nanothermometer is located within the 2nd BW. This scientific group presented the use of hybrid assemblies in the photothermal death of cancer cells while monitoring the *in situ* temperature. To track hybrid beads in 3D *in vitro* tumour spheroids, they registered the Nd^{3+} luminescence using an emission band at 1050 nm. Compared to 2D cell monolayers, 3D tumour spheroids more accurately capture the physiological and environmental characteristics of the tumour, such as particle penetration and cell resistance to temperature shock. They also investigated the local temperature in tumour spheroids during illumination and the associated cell survival rate by using luminescent NPs. As the camera records the temperature at the cell medium's surface, the NPs' temperature readings are constantly higher than the camera's, consistent with the crystals' sensitivity to the local temperature in the spheroid. This contrast shows how crucial it is to consider local heating for these applications. Furthermore, the results clearly define a life/death threshold, which in our case was set around 55 °C, by demonstrating a sharp temperature dependence of cell viability in spheroids.

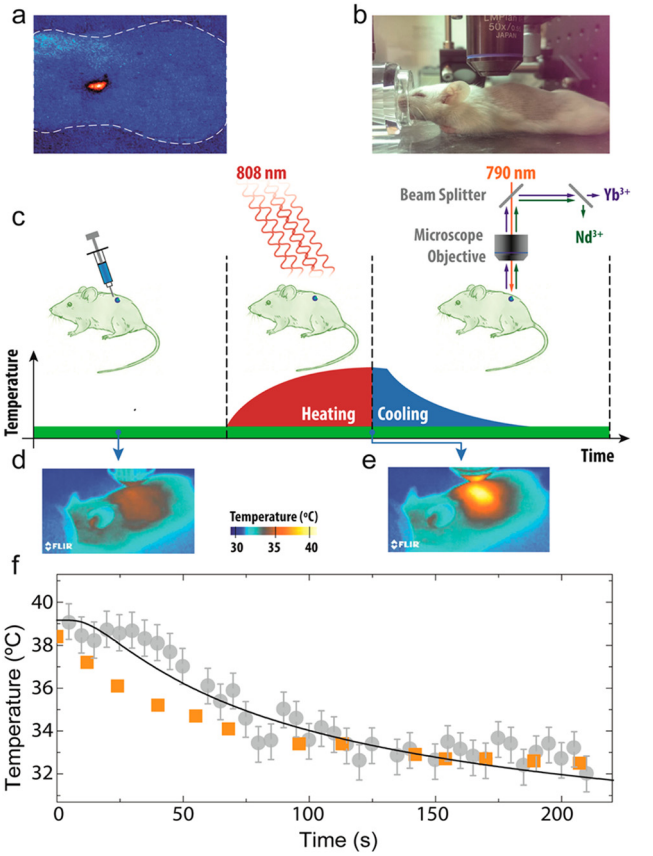

Fig. 12 (a) Fluorescence top-image of the CD1 mouse (delimited by the dashed line) where the subcutaneous injection of LaF_3:Nd^{3+}@LaF_3:Yb^{3+} NPs is evidenced by the bright fluorescence spot. (b) Digital picture of the CD1 mouse during *in vivo* thermal relaxation experiments. (c) Schematic representation of the subcutaneous thermal relaxation experiments. Thermal infrared images of the CD1 mouse before (d) and at the end (e) of the heating stimulus. (f) Time evolution of the temperatures measured by the subcutaneous luminescent thermometer (grey) and the IR thermal camera (orange). Dots are experimental subcutaneous (circles) and skin (squares) temperatures, whereas the solid line is the best fit. Reprinted with permission from ref. 95. Copyright (2016) American Chemical Society.

In contrast, Debasu *et al.*[72] were focused on the *in vitro* cell viability of MNT-1 melanoma and HeCaT cells incubated with Gd_2O_3:Nd^{3+} spherical NPs excited by an 808 nm laser. With both cell lines, the nanothermometers are biocompatible for NPs' concentrations up to 0.400 mg mL^{-1} and 24-hour exposure times. Both cell lines have a viability rate of more than 70%, which indicates that they are non-cytotoxic.

6.3. *Ex vivo* experiments

To reduce complications connected with *in vivo* and *in vitro* experiments, many studies initially employ phantom tissue (a preparation with optical absorption and scattering properties resembling those in real tissue) or *ex vivo* animal models, commonly using chicken breast, among others.[51] The use of

phantoms ensures high reproducibility of the experiments owing to their homogeneity and ability to control the shape and thickness of the sample. This level of control is not always achievable with *ex vivo* tissue. However, phantoms lack resemblance to the chemical environment of real tissues, necessitating *ex vivo* tissues. Chicken breast, being a homogeneous tissue with reduced absorption properties and providing sufficient thickness, is commonly chosen for studying laser penetration depth. However, it is important to note that commercial chicken breast exhibits significant variability in liquid retention, leading to variations in optical properties between samples. This variability can also affect the spread of injected luminescent nanomaterials and inaccuracies in temperature readout. To solve this problem, intramuscular injection without backflow into the chicken breast is essential for the effective delivery of NPs.[75]

Soares *et al.*[75] demonstrated that the presence of a chicken breast tissue had minimal effect on CaF_2:Yb^{3+},Er^{3+},Tm^{3+} emission at the 3rd BW. Therefore, it might be an optimal choice for subcutaneous luminescence detection.

Savchuk *et al.*[66] showed the possibility of using $KLu(WO_4)_2$:Tm^{3+},Ho^{3+} NPs in nanothermometry. The NPs emissions at 1480 and 1711 nm were selected for this experiment because their intensity ratio exhibited the highest thermal sensitivity when pumped at 808 nm. Bioimaging in *ex vivo* experiments was conducted by monitoring the heat from hot air in chicken meat, achieving a thermal resolution of approximately 0.5 °C and a penetration depth of at least 0.5 cm. The same group achieved a breast chicken penetration depth of 1 cm by observing $KGd(WO_4)_2$:Nd^{3+} emission at 1067 nm.[67] The fact that 1067 nm is situated at the 2nd BW, where there is less light absorption and scattering, can be the reason for the NIR emission's deep penetration into biological tissue.

In contrast, Benayas *et al.*[85] continuously monitored the luminescence of injected YAG:Nd^{3+} NPs into chicken breast tissue. A linear increase in subtissue temperature over time was observed during the heating process, reaching a maximum temperature change of approximately 55 °C. After stopping the hot air flow, thermal diffusion led to an exponential drop in temperature. These results proved that YAG:Nd^{3+} NPs can be used for online subtissue temperature monitoring.

Another group studying penetration depth was the Kolesnikov group.[56] They used phantom tissue of variable thickness and YVO_4:Nd^{3+} with the luminescence signal in the 2nd BW. The conducted experiment demonstrated that detecting the luminescence signal through 10 mm of human tissue is possible. They utilized a 2% aqueous intralipid emulsion to replicate the optical properties of human skin. Intralipid is an absorbing and scattering medium widely employed as phantom tissue in previous studies.[56] In another article, Kolesnikov *et al.*[91] used a colloidal solution of Y_2O_3:Nd^{3+} NPs (808 nm laser excitation) in the chicken breast at different depths to demonstrate the applicability of those NPs for temperature determination goals. They analysed the emission and calculated the LIR of the sub-tissue luminescence signal in the 2nd BW. The average temperature of 26.3 °C was discovered, which is extremely near the thermocouple-measured value of 26.5 °C. Notably, the thermal sensing error increases significantly with increasing tissue depth.

Ortgies *et al.*[8] analysed the luminescence generated by optomagnetic hybrid nanostructures (OMHSs) after passing through the chicken breast tissue. When subjecting the sample to an alternating magnetic field, the band intensity ratio experiences a slight increase, coupled with a small redshift of the emission band at approximately 864 nm. Analysing both the intensity ratio and spectral shift enables the determination of the temperature increment of the OMHSs as a function of the applied alternating magnetic field's intensity. Notably, thermal imaging disclosed a temperature increase of 11 °C, a value nearly identical to that determined by luminescence nanothermometry. Moreover, they conducted additional *ex vivo* experiments on lamb hearts to showcase the potential of OMHSs for fully controlled photothermal therapies. To measure the heating of the coronary wall caused by the laser, they captured the emission spectrum at different laser powers of 808 nm. The laser-induced temperature increment obtained is as substantial as 50 °C, even for a moderate laser power of 35 mW, which is significant to induce both hyperthermia and tissue ablation. In conclusion, the combination of optical and magnetic heating in opto-magnetic NPs and the possibility of real-time thermal control presents a promising opportunity to bring such therapeutic applications closer to the point of clinical application.

Quintanilla *et al.* tested CaF_2:Nd^{3+},Y^{3+} NPs for subtissue thermometry experiments using gold nanorods as nanoheaters.[58] This scientific group proved that the thermal resolution achieved in experiments depends highly on tissue thickness, ranging between 0.2 and 3.5 °C. The tissue fragments ranging in thickness up to 7 mm were used to measure the solution's temperature.

In turn, Marciniak *et al.*[57] injected the colloidal solution of $LiNdP_4O_{12}$ NPs at different chicken breast depths and estimated the excitation line's penetration depth and emission from NPs at 30 mm. Moreover, they observed the NPs' emission in the HEK cells.

Rocha *et al.*[78] carried out the *ex vivo* experiments and concluded that LaF_3:Nd^{3+} NPs are capable of real-time sub-tissue thermal readings with a temperature resolution of 0.7 °C (Fig. 13). In another article, they presented single-beam sub-tissue-controlled heating process (subtissue hyperthermia process) based on the combination of LaF_3:Nd^{3+} NPs and gold nanorods, which function as nanothermometers and nanoheaters, respectively.[65] They measured the NPs emission as a function of the thickness of phantom tissue and found the subtissue penetration lengths to be close to 2 mm.

The heating–cooling dynamics of $LiLuF_4$:Nd^{3+} NPs distributed in water through different thicknesses (1–5 mm) of pork fat tissues were examined by Skripka *et al.*[59] The results showed that transient temperature measurements through tissue can be employed to monitor rapid temperature changes at a tissue depth of 3 mm. In contrast, slower temperature changes can be measured at even greater depths. The photoluminescence at approximately 1050 nm, associated with the $^4F_{3/2} \rightarrow {}^4I_{11/2}$ transition, was the most reliable and appropriate wavelength for thermal readings.

Pereira *et al.*[60] checked the influence of scattering and water absorption on the penetration length of 800 nm and 1319 nm wavelengths in chicken pectoral muscle. Based on those *ex vivo*

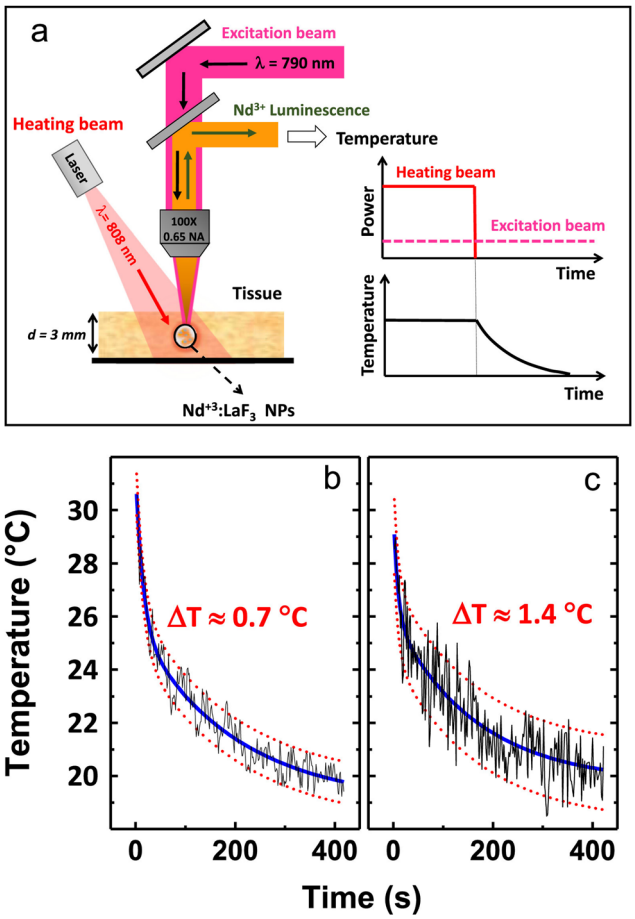

Fig. 13 (a) Schematic representation of the *ex vivo* subtissue time-resolved thermal sensing experiments. Two laser beams are used, one of them for heating (modulated heating beam) and the second one (the excitation beam) for continuous excitation of the subtissue injected LaF_3:Nd^{3+} NPs. (b) and (c) Correspond to the time evolution curves of the sub-tissue temperature after switching off the 808 nm heating laser beam as obtained from the analysis of the 861 nm to 863 nm and 885 nm to 865 nm intensity ratio, respectively. Blue solid lines indicate average values, whereas red dashes are graphic indications of temperature uncertainties extracted from experimental data. Reprinted from ref. 78; Copyright (2016), with permission from Elsevier.

experiments, they estimated the penetration lengths to be 2.3 mm and 1.1 mm for 1319 nm and 800 nm, respectively. Therefore, by combining the results at 800 nm and 1319 nm, it can be asserted that a penetration depth as large as 3 mm is achievable.

Li *et al.*[96] suggested that different tissue components are transmitted differently by the NIR emission of Ba_2LuF_7:Yb^{3+}, Nd^{3+},Er^{3+}@Ba_2LaF_7 NPs, which enables imaging of foreign bodies within chicken tissues, *i.e.* ribs and cartilage tissue were visible in 4 and 6 mm thick tissue imaging. Moreover, imaging the human pinky finger still permits a reasonably clear view of the bones and joints, suggesting that studied NPs may be helpful in deep tissue imaging.

Xu *et al.*[94] demonstrated that the light emission in the 2nd BW can penetrate a 4 mm thick chicken breast tissue with only a 30% decrease. Therefore, the designed $NaYF_4$:Yb^{3+},Ho^{3+}@$NaYF_4$:Yb^{3+},Er^{3+}@$NaNdF_4$:Yb^{3+} NPs have a high potential for superficial subcutaneous tissue NIR imaging. They also checked the cytotoxicity of those NPs using the MTT test. Upon increasing the concentration of NPs to 250 μg mL^{-1}, HeLa cells do not exhibit any noticeable apoptosis, which indicates negligible cytotoxicity of those NPs.

In another study, Gschwend *et al.* demonstrated the potential of $BiVO_4$:Nd^{3+} nanothermometers for temperature measurements within biological tissues such as chicken skeletal muscle.[71] The FIR method was used to measure the temperature of the nanothermometers through the tissue at a wavelength of 750 nm laser excitation. Meanwhile, thermal imaging was used to measure the surface temperatures of the tissue. In less than 900 seconds, the control particles and nanothermometer temperature rose to 78 °C. The surface temperature rises much more slowly, taking 15 minutes to reach 51 °C, which gives a 27 °C temperature difference. The final temperature difference was 23 and 33 °C, corresponding to 1.5- and 6-mm thick tissues. The presented studies reveal that nanothermometers are reliable even when used with scattering and absorbing materials like chicken tissue.

Porosnicu *et al.*[103] calculated the thermal sensitivity based on the lifetime temperature dependence of the Y_2O_3:Ho^{3+},Er^{3+},Yb^{3+} NIR emissions at 1200 and 1530 nm, respectively. The maximum relative sensitivity was approximately 0.4% $°C^{-1}$ at room temperature due to the lifetime decrease of Ho^{3+} emission by temperature, whereas the maximum relative sensitivity of 0.6% $°C^{-1}$ at 87 °C was obtained for Er^{3+} lifetime thermometry. Additionally, $LIR_{Er/Ho}$ demonstrates outstanding stability over time, maintaining a negligible local heating effect with a standard error of only 0.2%.

Nexha *et al.*[74] used an 808 nm laser with a power of 200 mW in the presented studies and did not observe degradation or burning of the surface of a chicken breast, which was used for testing the $KLu(WO_4)_2$:Ho^{3+},Tm^{3+} NPs. The researchers estimated that the difference between the temperature indicated by NPs and thermocouples was just 0.8 °C.

Notably, luminescent thermometers can work in challenging environments like biological fluids, intense electromagnetic fields, cryogenic temperatures, and rapidly moving objects without affecting their resolution.[123] Therefore, a wide range of internal organ-related therapeutic and diagnostic applications may benefit from the use of such materials.[56,126]

7. Summary and perspectives

Nanothermometry based on the spectroscopic properties of lanthanide ions is rapidly developing in recent years. Currently, a wide range of nanomaterials with different compositions, doped with various Ln^{3+} ions, exhibit decent relative sensitivities that allow their application in real-world scenarios. Among the significant achievements in optical nanothermometry are the generation of luminescent signals within the biological windows and the testing of thermosensitive properties not only in colloidal systems but also *in vitro, ex vivo* and, most importantly, *in vivo*.

While challenges remain in incorporating temperature sensors into living organisms, it has been demonstrated that nanomaterials doped with Ln^{3+} ions fulfil their purpose and enable temperature detection. On the other hand, developing

primary thermometers, which do not require temperature recalibration (*i.e.*, allow determination of temperature exclusively based on the first principles of Boltzmann distribution – thermal equilibrium) and entirely operating within the BWs, is still challenging. The primary thermometers should have a well-defined relationship between the thermometric parameter and k_BT.[10] However, such luminescent thermometers have limited relative sensitivity, which is strictly associated with the energy separation (ΔE) between the thermally-coupled levels. Another often underestimated problem, which occurs in the case of ratiometric thermometers, is a significant reabsorption and light scattering of the incident and emitted photons, introducing erroneous temperature readouts during the measurements in real, biological systems, where the presence of surrounding media is inherent. The proper understanding of physical mechanisms governing the observed temperature-induced changes of spectroscopic parameters is another issue, limiting the full potential of the developed luminescent thermometers. One should also consider the long-lasting cytotoxicity issues associated with introducing nanoparticles into the living organism.

Based on the collected literature here, the composition of nanomaterials is not a limitation for potential applications. Scientists utilize various inorganic matrices such as oxide systems like $Y_3Al_5O_{12}$ garnet structures,[69] phosphates like $LaPO_4$,[92] YVO_4 vanadates,[64] $KGd(WO_4)_2$ tungstates,[67] and many others. However, fluorides appear to be the most promising and biocompatible, exhibiting low phonon energies and favourable morphology, often superior to materials obtained through high-temperature annealing.

Additionally, fluoride-based NPs can be obtained as core@shell structures, significantly enhancing emission intensity and insulating the core from the surface, including molecules that improve biocompatibility. Fluoride-based NPs can also be produced as multi-layered particles, allowing the use of different dopant ion concentrations, as seen in $NaNdF_4$@$NaYF_4$@$NaYF_4$:Nd^{3+} NPs,[59] or utilizing the emission of different Ln^{3+} ions that, if in the same phase, would undergo quenching, as in $NaYF_4$:Yb^{3+},Ho^{3+}@$NaYF_4$:Yb^{3+},Er^{3+}@$NaNdF_4$:Yb^{3+}.[94]

Two phenomena can be exploited when designing nanothermometers for biological applications: down-shifting and upconversion. Down-shifting involves exciting with a laser of a suitable wavelength, often within the 760–830 nm range, utilizing the sensitizing properties of Nd^{3+} ions to generate luminescent signals within the BWs. Upconversion typically involves excitation in the 2nd or 3rd BW with simultaneous emission in the 1st BW. Also, both phenomena can be used simultaneously to observe how the emitted signals change with temperature.

Among the most commonly used dopant ions in nanomaterials are Nd^{3+} ions. Many publications focusing on medical applications of nanothermometry exploit the fact that Nd^{3+} ions can be excited within the 1st BW by a laser with a wavelength of 808 nm. However, due to the spectroscopic properties of Nd^{3+} ions, the relative sensitivity of nanothermometers based on them usually does not exceed 0.5% $^\circ C^{-1}$, resulting from using Stark levels with small energy separation. Promising applications involve using Nd^{3+} ions as sensitizers to transfer energy and excite other dopant ions like Er^{3+} or Ho^{3+}, whose emission is then used for temperature detection. The sensitivity of such thermometers typically falls within the range of 1–2.5% $^\circ C^{-1}$.

For upconversion-based nanothermometers, Tm^{3+} ions appear to be the most promising sensitizers. They allow excitation with radiation in the 2nd BW, around 1210 nm.[108,114] Additionally, the emission of Tm^{3+} ions occurs within the 1st BW (around 800 nm), and these ions can transfer the absorbed energy to other ions, such as Er^{3+}, increasing the number of emission bands available for temperature detection.

As mentioned earlier, nanothermometers based on the emission of Ln^{3+} ions also have their limitations, not only related to the energy separation between the thermally-coupled levels. A significant challenge in achieving intense luminescence, both down-shifting and upconversion, is the low molar absorption coefficient of Ln^{3+} ions. This is due to the partially forbidden nature of f–f electronic transitions, which necessitates using lasers to observe nanoparticle emission. Various efforts are being made in this direction, such as designing core@shell nanoparticle architectures and optimizing the concentration and distribution of dopant ions within the nanoparticles. The lasers used are often of relatively high power density; however, many cited scientific publications have not conducted experiments *ex vivo* or *in vivo* at power densities <0.5 W cm^{-2}, which poses a challenge for the potential application of the studied nanoparticles.

Certainly, many more research studies need to be conducted to obtain ideal nanoparticles. One of the most important development directions in the field of nanothermometry based on Ln^{3+} ions is the pursuit of achieving intense emission (high quantum efficiency of emission) when excited by radiation within the biological windows and obtaining high values of nanothermometers sensitivity in the physiological temperature range. It is also important for nanothermometers to be studied in terms of the conversion of the exciting radiation energy into heat (optical heating), which is still rarely addressed in published studies. Furthermore, for biomedical applications, it is crucial to determine the nanoparticles' toxicity and investigate what may happen to the decomposition products of the nanoparticles within the body.

In summary, optical nanothermometry based on the properties of Ln^{3+} ions is one of the best methods for remote temperature detection, with the main potential application in nanomedicine. The properties of Ln^{3+} ions allow the design of nanothermometers with required features, such as optimal excitation and emission wavelengths, as well as relative sensitivity. Nanothermometry is gaining attention from an increasing number of research groups worldwide, promising the development of NPs with even greater sensitivity than those known to date, capable of detecting emissions from deeper tissues than the reported ranges, reaching beyond millimetres to centimetres.

Besides the further development and continuation of the works discussed in this review, there are other great perspectives for the use of lanthanide-based luminescence nanothermometry for sensing in biological systems. Such future directions in this field may encompass, *e.g.* excitation in the 2nd BW and down-shifting emission in the 3rd BW; excitation in the 3rd BW and

observations of UC emission in the 2nd BW; non-linear down-conversion/quantum cutting phenomena from the 1st to 3rd BW. Utilizing the processes mentioned above, one could remotely monitor temperature gradient in various biological systems operating with single or multiple thermometric parameters, including luminescence intensity, LIR, band shift, FWHM and lifetimes. Multi-parameter thermal sensing combined with automatic data processing based on artificial intelligence, machine learning and neural networks may significantly improve the accuracy and precision of temperature detection. Moreover, the employment of two-dimensional (2D) and three-dimensional (3D) thermal mapping may boost the development of modern nano-biomedicine, allowing precise localisation (spatial recognition) of the inflammation-affected tissues, followed by targeted drug delivery and localized photodynamic therapy (PDT). It is worth noting about other emerging strategies for temperature sensing, which could also be employed in this field, *i.e.*, a combination of lanthanide luminescence with a non-linear, parametric process of second harmonic generation (SHG) in nanomaterials, in which the intensity ratio of Stokes or anti-Stokes emission of Ln^{3+} ions to the SHG signal can be employed as thermometric parameter.[145,146]

Author contributions

Natalia Jurga – conceptualization, visualization, writing – original draft, writing – review & editing; Marcin Runowski – conceptualization, writing – original draft, writing – review & editing; Tomasz Grzyb – conceptualization, writing – original draft, writing – review & editing.

Data availability

No primary research results, software or code have been included and no new data were generated or analysed as part of this review.

Conflicts of interest

There are no conflicts to declare.

References

1 P. R. N. Childs, J. R. Greenwood and C. A. Long, *Rev. Sci. Instrum.*, 2000, **71**, 2959–2978.
2 M. R. Moldover, W. L. Tew and H. W. Yoon, *Nat. Phys.*, 2016, **12**, 7–11.
3 S. W. Allison and G. T. Gillies, *Rev. Sci. Instrum.*, 1997, **68**, 2615–2650.
4 K. Okabe, N. Inada, C. Gota, Y. Harada, T. Funatsu and S. Uchiyama, *Nat. Commun.*, 2012, **3**, 705.
5 D. Jaque, L. Martínez Maestro, B. del Rosal, P. Haro-Gonzalez, A. Benayas, J. L. Plaza, E. Martín Rodríguez and J. García Solé, *Nanoscale*, 2014, **6**, 9494–9530.
6 Y. Il Park, H. M. Kim, J. H. Kim, K. C. Moon, B. Yoo, K. T. Lee, N. Lee, Y. Choi, W. Park, D. Ling, K. Na, W. K. Moon, S. H. Choi, H. S. Park, S.-Y. Yoon, Y. D. Suh, S. H. Lee and T. Hyeon, *Adv. Mater.*, 2012, **24**, 5755–5761.
7 J. Xu, L. Xu, C. Wang, R. Yang, Q. Zhuang, X. Han, Z. Dong, W. Zhu, R. Peng and Z. Liu, *ACS Nano*, 2017, **11**, 4463–4474.
8 D. H. Ortgies, F. J. Teran, U. Rocha, L. de la Cueva, G. Salas, D. Cabrera, A. S. Vanetsev, M. Rähn, V. Sammelselg, Y. V. Orlovskii and D. Jaque, *Adv. Funct. Mater.*, 2018, **28**, 1–11.
9 C. D. S. Brites, A. Millán and L. D. Carlos, *Handbook on the Physics and Chemistry of Rare Earths*, 2016, vol. 49, pp. 339–427.
10 C. D. S. Brites, R. Marin, M. Suta, A. N. Carneiro Neto, E. Ximendes, D. Jaque and L. D. Carlos, *Adv. Mater.*, 2023, **35**, 2302749.
11 D. Jaque and F. Vetrone, *Nanoscale*, 2012, **4**, 4301–4326.
12 M. D. Dramićanin, *J. Appl. Phys.*, 2020, **128**, 040902.
13 M. Quintanilla, I. X. Cantarelli, M. Pedroni, A. Speghini and F. Vetrone, *J. Mater. Chem. C*, 2015, **3**, 3108–3113.
14 M. Runowski, A. Shyichuk, A. Tymiński, T. Grzyb, V. Lavín and S. Lis, *ACS Appl. Mater. Interfaces*, 2018, **10**, 17269–17279.
15 S. Goderski, M. Runowski, P. Woźny, V. Lavín and S. Lis, *ACS Appl. Mater. Interfaces*, 2020, **12**, 40475–40485.
16 E. C. Ximendes, U. Rocha, T. O. Sales, N. Fernández, F. Sanz-Rodríguez, I. R. Martín, C. Jacinto and D. Jaque, *Adv. Funct. Mater.*, 2017, **27**, 1702249.
17 M. Runowski, *Handbook of Nanomaterials in Analytical Chemistry*, Elsevier, 2020, pp. 227–273.
18 A. Bednarkiewicz, J. Drabik, K. Trejgis, D. Jaque, E. Ximendes and L. Marciniak, *Appl. Phys. Rev.*, 2021, **8**, 011317.
19 L. Marciniak, K. Kniec, K. Elżbieciak-Piecka, K. Trejgis, J. Stefanska and M. Dramićanin, *Coord. Chem. Rev.*, 2022, **469**, 214671.
20 L. Labrador-Páez, M. Pedroni, A. Speghini, J. García-Solé, P. Haro-González and D. Jaque, *Nanoscale*, 2018, **10**, 22319–22328.
21 N. Stopikowska, P. Woźny, M. Suta, T. Zheng, S. Lis and M. Runowski, *J. Mater. Chem. C*, 2023, **11**, 9620–9627.
22 S. Choi, V. N. Agafonov, V. A. Davydov and T. Plakhotnik, *ACS Photonics*, 2019, **6**, 1387–1392.
23 T. Zheng, M. Sójka, M. Runowski, P. Woźny, S. Lis and E. Zych, *Adv. Opt. Mater.*, 2021, **9**, 2101507.
24 F. E. Maturi, C. D. S. Brites, E. C. Ximendes, C. Mills, B. Olsen, D. Jaque, S. J. L. Ribeiro and L. D. Carlos, *Laser Photonics Rev.*, 2021, **15**, 2100301.
25 W. Zheng, P. Huang, D. Tu, E. Ma, H. Zhu and X. Chen, *Chem. Soc. Rev.*, 2015, **44**, 1379–1415.
26 K. Binnemans, *Chem. Rev.*, 2009, **109**, 4283–4374.
27 B. G. Wybourne and L. Smentek, *Optical spectroscopy of lanthanides*, CRC Press, New York, 2007.
28 J.-C. G. Bünzli, *Eur. J. Inorg. Chem.*, 2017, 5058–5063.
29 J.-C. G. Bünzli, *Trends Chem.*, 2019, **1**, 751–762.
30 Y. Liu, Y. Lu, X. Yang, X. Zheng, S. Wen, F. Wang, X. Vidal, J. Zhao, D. Liu, Z. Zhou, C. Ma, J. Zhou, J. A. Piper, P. Xi and D. Jin, *Nature*, 2017, **543**, 229–233.
31 D. J. Garfield, N. J. Borys, S. M. Hamed, N. A. Torquato, C. A. Tajon, B. Tian, B. Shevitski, E. S. Barnard, Y. D. Suh, S. Aloni, J. B. Neaton, E. M. Chan, B. E. Cohen and P. J. Schuck, *Nat. Photonics*, 2018, **12**, 402–407.

32 J. Zhou, Z. Liu and F. Li, *Chem. Soc. Rev.*, 2012, **41**, 1323–1349.
33 X. Liu, C.-H. Yan and J. A. Capobianco, *Chem. Soc. Rev.*, 2015, **44**, 1299–1301.
34 M.-K. Tsang, G. Bai and J. Hao, *Chem. Soc. Rev.*, 2015, **44**, 1585–1607.
35 F. Auzel, *Chem. Rev.*, 2004, **104**, 139–174.
36 A. Nadort, J. Zhao and E. M. Goldys, *Nanoscale*, 2016, **8**, 13099–13130.
37 G. Wang, Q. Peng and Y. Li, *Acc. Chem. Res.*, 2011, **44**, 322–332.
38 Y. Liu, D. Tu, H. Zhu and X. Chen, *Chem. Soc. Rev.*, 2013, **42**, 6924.
39 M. Quintanilla, A. Benayas, R. Naccache and F. Vetrone, *Thermometry at the Nanoscale: Techniques and Selected Applications*, 2015, pp. 124–166.
40 M. Kamimura, T. Matsumoto, S. Suyari, M. Umezawa and K. Soga, *J. Mater. Chem. B*, 2017, **5**, 1917–1925.
41 E. C. Ximendes, U. Rocha, K. U. Kumar, C. Jacinto and D. Jaque, *Appl. Phys. Lett.*, 2016, **108**, 253103.
42 C. D. S. Brites, B. Zhuang, M. L. Debasu, D. Ding, X. Qin, F. E. Maturi, W. W. Y. Lim, D. W. Soh, J. Rocha, Z. Yi, X. Liu and L. D. Carlos, *J. Phys. Chem. Lett.*, 2020, **11**, 6704–6711.
43 A. R. N. Bastos, C. D. S. Brites, P. A. Rojas-Gutierrez, C. DeWolf, R. A. S. Ferreira, J. A. Capobianco and L. D. Carlos, *Adv. Funct. Mater.*, 2019, **29**, 1905474.
44 A. Bednarkiewicz, L. Marciniak, L. D. Carlos and D. Jaque, *Nanoscale*, 2020, **12**, 14405–14421.
45 A. M. Smith, M. C. Mancini and S. Nie, *Nat. Nanotechnol.*, 2009, **4**, 710–711.
46 S. Diao, J. L. Blackburn, G. Hong, A. L. Antaris, J. Chang, J. Z. Wu, B. Zhang, K. Cheng, C. J. Kuo and H. Dai, *Angew. Chem.*, 2015, **127**, 14971–14975.
47 E. Hemmer, A. Benayas, F. Légaré and F. Vetrone, *Nanoscale Horiz.*, 2016, **1**, 168–184.
48 M. D. Shinn, W. A. Sibley, M. G. Drexhage and R. N. Brown, *Phys. Rev. B: Condens. Matter Mater. Phys.*, 1983, **27**, 6635–6648.
49 M. Runowski, P. Wozny, N. Stopikowska, I. R. Martín, V. Lavín and S. Lis, *ACS Appl. Mater. Interfaces*, 2020, **12**, 43933–43941.
50 C. D. S. Brites, K. Fiaczyk, J. F. C. B. Ramalho, M. Sójka, L. D. Carlos and E. Zych, *Adv. Opt. Mater.*, 2018, **6**, 1701318.
51 M. Runowski, S. Goderski, D. Przybylska, T. Grzyb, S. Lis and I. R. Martín, *ACS Appl. Nano Mater.*, 2020, **3**, 6406–6415.
52 N. Stopikowska, M. Runowski, M. Skwierczyńska and S. Lis, *Nanoscale*, 2021, **13**, 14139–14146.
53 D. Przybylska and T. Grzyb, *J. Alloys Compd.*, 2020, **831**, 154797.
54 N. Jurga, S. Ryszczyńska and T. Grzyb, *Spectrochim. Acta, Part A*, 2023, **303**, 123220.
55 A. Skripka, A. Benayas, R. Marin, P. Canton, E. Hemmer and F. Vetrone, *Nanoscale*, 2017, **9**, 3079–3085.
56 I. E. Kolesnikov, E. V. Golyeva, M. A. Kurochkin, E. Lähderanta and M. D. Mikhailov, *Sens. Actuators, B*, 2016, **235**, 287–293.
57 L. Marciniak, K. Prorok, A. Bednarkiewicz, A. Kowalczyk, D. Hreniak and W. Strek, *J. Lumin.*, 2016, **176**, 144–148.
58 M. Quintanilla, Y. Zhang and L. M. Liz-Marzán, *Chem. Mater.*, 2018, **30**, 2819–2828.
59 A. Skripka, A. Morinvil, M. Matulionyte, T. Cheng and F. Vetrone, *Nanoscale*, 2019, **11**, 11322–11330.
60 A. F. Pereira, J. F. Silva, A. S. Gouveia-Neto and C. Jacinto, *Sens. Actuators, B*, 2017, **238**, 525–531.
61 Y. Shen, J. Lifante, N. Fernández, D. Jaque and E. Ximendes, *ACS Nano*, 2020, **14**, 4122–4133.
62 L. Wu, M. Jia, D. Li and G. Chen, *Nano Lett.*, 2023, **23**, 2862.
63 P. Cortelletti, C. Facciotti, I. X. Cantarelli, P. Canton, M. Quintanilla, F. Vetrone, A. Speghini and M. Pedroni, *Opt. Mater.*, 2017, **68**, 29–34.
64 I. E. Kolesnikov, A. A. Kalinichev, M. A. Kurochkin, E. V. Golyeva, E. Y. Kolesnikov, A. V. Kurochkin, E. Lähderanta and M. D. Mikhailov, *Sci. Rep.*, 2017, **7**, 18002.
65 U. Rocha, C. Jacinto da Silva, W. Ferreira Silva, I. Guedes, A. Benayas, L. Martínez Maestro, M. Acosta Elias, E. Bovero, F. C. J. M. van Veggel, J. A. García Solé and D. Jaque, *ACS Nano*, 2013, **7**, 1188–1199.
66 O. A. Savchuk, J. J. Carvajal, P. Haro-Gonzalez, M. Aguiló and F. Díaz, *J. Alloys Compd.*, 2018, **746**, 710–719.
67 O. Savchuk, J. J. Carvajal, L. G. De la Cruz, P. Haro-González, M. Aguiló and F. Díaz, *J. Mater. Chem. C*, 2016, **4**, 7397–7405.
68 M. Quintanilla, I. García, I. de Lázaro, R. García-Alvarez, M. Henriksen-Lacey, S. Vranic, K. Kostarelos and L. M. Liz-Marzán, *Theranostics*, 2019, **9**, 7298–7312.
69 A. Cantarano, J. Yao, M. Matulionyte, J. Lifante, A. Benayas, D. H. Ortgies, F. Vetrone, A. Ibanez, C. Gérardin, D. Jaque and G. Dantelle, *ACS Appl. Mater. Interfaces*, 2020, **12**, 51273–51284.
70 K. Maciejewska and L. Marciniak, *Sci. Rep.*, 2023, **13**, 1–8.
71 P. M. Gschwend, F. H. L. Starsich, R. C. Keitel and S. E. Pratsinis, *Chem. Commun.*, 2019, **55**, 7147–7150.
72 M. L. Debasu, H. Oliveira, J. Rocha and L. D. Carlos, *J. Rare Earths*, 2020, **38**, 483–491.
73 Q. Hu, N. Kong, Y. Chai, Z. Xing, Y. Wu, J. Zhang, F. Li and X. Zhu, *Nanoscale Horiz.*, 2022, **7**, 1177–1185.
74 A. Nexha, J. J. Carvajal, M. C. Pujol, F. Díaz and M. Aguiló, *J. Mater. Chem. C*, 2020, **8**, 180–191.
75 A. C. C. Soares, T. O. Sales, E. C. Ximendes, D. Jaque and C. Jacinto, *Nanoscale Adv.*, 2023, **5**, 3664–3670.
76 D. Chen, Y. Liang, S. Miao, J. Bi and K. Sun, *J. Lumin.*, 2021, **234**, 117967.
77 A. D. Lozano-Gorrín, U. R. Rodríguez-Mendoza, V. Venkatramu, V. Monteseguro, M. A. Hernández-Rodríguez, I. R. Martín and V. Lavín, *Opt. Mater.*, 2018, **84**, 46–51.
78 U. Rocha, C. Jacinto, K. U. Kumar, F. J. López, D. Bravo, J. G. Solé and D. Jaque, *J. Lumin.*, 2016, **175**, 149–157.
79 D. Wawrzynczyk, A. Bednarkiewicz, M. Nyk, W. Strek and M. Samoc, *Nanoscale*, 2012, **4**, 6959.
80 L. Marciniak, A. Pilch, S. Arabasz, D. Jin and A. Bednarkiewicz, *Nanoscale*, 2017, **9**, 8288–8297.
81 P. Huang, W. Zheng, D. Tu, X. Shang, M. Zhang, R. Li, J. Xu, Y. Liu and X. Chen, *Adv. Sci.*, 2019, **6**, 1–7.
82 E. P. Santos, R. S. Pugina, E. G. Hilário, A. J. A. Carvalho, C. Jacinto, F. A. M. G. Rego-Filho, A. Canabarro, A. S. L. Gomes, J. M. A. Caiut and A. L. Moura, *Sens. Actuators, A*, 2023, **362**, 114666.

83 E. Carrasco, B. Del Rosal, F. Sanz-Rodríguez, Á. J. De La Fuente, P. H. Gonzalez, U. Rocha, K. U. Kumar, C. Jacinto, J. G. Solé and D. Jaque, *Adv. Funct. Mater.*, 2015, **25**, 615–626.
84 L. Marciniak, A. Bednarkiewicz, D. Hreniak and W. Strek, *J. Mater. Chem. C*, 2016, **4**, 11284–11290.
85 A. Benayas, B. del Rosal, A. Pérez-Delgado, K. Santacruz-Gómez, D. Jaque, G. A. Hirata and F. Vetrone, *Adv. Opt. Mater.*, 2015, **3**, 687–694.
86 G. Dantelle, M. Matulionyte, D. Testemale, A. Cantarano, A. Ibanez and F. Vetrone, *Phys. Chem. Chem. Phys.*, 2019, **21**, 11132–11141.
87 W. S. Silva, A. C. A. Silva, U. Rocha, N. O. Dantas, W. F. Silva and C. Jacinto, *Sens. Actuators, A*, 2021, **317**, 112445.
88 L. H. A. R. Ferreira, G. Dantelle, A. Ibanez and L. J. Q. Maia, *Phys. B*, 2022, **644**, 414193.
89 C. Renero-Lecuna, A. Herrero, D. Jimenez de Aberasturi, M. Martínez-Flórez, R. Valiente, M. Mychinko, S. Bals and L. M. Liz-Marzán, *J. Phys. Chem. C*, 2021, **125**, 19887–19896.
90 S. Balabhadra, M. L. Debasu, C. D. S. Brites, J. Rocha and L. D. Carlos, *J. Lumin.*, 2016, **180**, 25–30.
91 I. E. Kolesnikov, A. A. Kalinichev, M. A. Kurochkin, D. V. Mamonova, E. Y. Kolesnikov, A. V. Kurochkin, E. Lähderanta and M. D. Mikhailov, *J. Lumin.*, 2018, **204**, 506–512.
92 K. Maciejewska, A. Bednarkiewicz and L. Marciniak, *Phys. B*, 2021, **620**, 413247.
93 N. Rakov, Y. Xing and G. S. Maciel, *ACS Appl. Nano Mater.*, 2020, **3**, 10479–10486.
94 H. Xu, M. Jia, Z. Wang, Y. Wei and Z. Fu, *ACS Appl. Mater. Interfaces*, 2021, **13**, 61506–61517.
95 E. C. Ximendes, W. Q. Santos, U. Rocha, U. K. Kagola, F. Sanz-Rodríguez, N. Fernández, A. D. S. Gouveia-Neto, D. Bravo, A. M. Domingo, B. del Rosal, C. D. S. Brites, L. D. L. D. Carlos, D. Jaque, C. Jacinto, U. Rocha Silva, K. U. Kumar, F. Sanz Rodríguez, N. Fernández, A. da S. Gouveia Neto, D. Bravo, A. Martín Domingo, B. del Rosal, C. D. S. Brites, L. D. L. D. Carlos, D. Jaque and C. Jacinto, *Nano Lett.*, 2016, **16**, 1695.
96 H. Li, E. Heydari, Y. Li, H. Xu, S. Xu, L. Chen and G. Bai, *Nanomaterials*, 2023, **13**, 219.
97 H. Wei, F. Cui, W. Guo, R. Ye and L. Lei, *Opt. Mater.*, 2022, **124**, 112016.
98 Z. Ji, Y. Cheng, X. Cui, H. Lin, J. Xu and Y. Wang, *Inorg. Chem. Front.*, 2019, **6**, 110–116.
99 M. Tan, F. Li, N. Cao, H. Li, X. Wang, C. Zhang, D. Jaque and G. Chen, *Small*, 2020, **16**, 1–10.
100 G. López-Peña, K. Hamraoui, K. Horchani-Naifer, C. Gerke, D. H. Ortgies, E. Martín Rodríguez, G. Chen, D. Jaque and J. Rubio Retama, *Phys. B*, 2022, **631**, 0–6.
101 C. Hazra, A. Skripka, S. J. L. Ribeiro and F. Vetrone, *Adv. Opt. Mater.*, 2020, **8**, 1–9.
102 Y. Wang, L. Lei, E. Liu, Z. Lu and S. Xu, *Opt. Commun.*, 2022, **510**, 127935.
103 I. Porosnicu, C. Colbea, F. Baiasu, M. Lungu, M. C. Istrate, D. Avram and C. Tiseanu, *Methods Appl. Fluoresc.*, 2020, **8**, 035005.
104 G. Xiang, X. Liu, J. Zhang, Z. Liu, W. Liu, Y. Ma, S. Jiang, X. Tang, X. Zhou, L. Li and Y. Jin, *Inorg. Chem.*, 2019, **58**, 8245–8252.
105 S. Liu, Z. An, J. Huang and B. Zhou, *Nano Res.*, 2023, **16**, 1626–1633.
106 S. Liu, Z. An, J. Huang and B. Zhou, *Nano Res.*, 2023, **16**, 1626–1633.
107 T. Grzyb, P. Kamiński, D. Przybylska, A. Tymiński, F. Sanz-Rodríguez and P. Haro Gonzalez, *Nanoscale*, 2021, **13**, 7322–7333.
108 P. R. Grzyb Tomasz and R. Martín Inocencio, *Nanoscale*, 2024, **16**, 1692.
109 E. M. Mettenbrink, W. Yang and S. Wilhelm, *Adv. Photonics Res.*, 2022, **3**, 2200098.
110 X. Zheng, R. K. Kankala, C. G. Liu, S. Bin Wang, A. Z. Chen and Y. Zhang, *Coord. Chem. Rev.*, 2021, **438**, 213870.
111 M. R. Hamblin, *Dalton Trans.*, 2018, **47**, 8571–8580.
112 P. A. Rojas-Gutierrez, S. Bhuckory, C. Mingoes, N. Hildebrandt, C. Dewolf and J. A. Capobianco, *ACS Appl. Nano Mater.*, 2018, **1**, 5345–5354.
113 S. Ryszczyńska, I. R. Martín and T. Grzyb, *Sci. Rep.*, 2023, **13**, 14819.
114 M. A. Hernández-Rodriguez, A. D. Lozano-Gorrín, V. Lavín, U. R. Rodríguez-Mendoza and I. R. Martín, *Opt. Express*, 2017, **25**, 27845.
115 S. Ryszczyńska, K. Trejgis, Ł. Marciniak and T. Grzyb, *ACS Appl. Nano Mater.*, 2021, **4**, 10438–10448.
116 C. Würth, B. Grauel, M. Pons, F. Frenzel, P. Rissiek, K. Rücker, M. Haase and U. Resch-Genger, *Nano Res.*, 2022, **15**, 9639–9646.
117 L. Marciniak, A. Bednarkiewicz and K. Elzbieciak, *J. Mater. Chem. C*, 2018, **6**, 7568–7575.
118 K. Trejgis, K. Maciejewska, A. Bednarkiewicz and L. Marciniak, *ACS Appl. Nano Mater.*, 2020, **3**, 4818–4825.
119 K. Trejgis, K. Ledwa, L. Li and L. Marciniak, *J. Mater. Chem. C*, 2022, **10**, 3006–3014.
120 A. M. Kotulska, K. Prorok and A. Bednarkiewicz, *Methods Appl. Fluoresc.*, 2019, **7**, 034001.
121 E. S. Levy, C. A. Tajon, T. S. Bischof, J. Iafrati, A. Fernandez-Bravo, D. J. Garfield, M. Chamanzar, M. M. Maharbiz, V. S. Sohal, P. J. Schuck, B. E. Cohen and E. M. Chan, *ACS Nano*, 2016, **10**, 8423–8433.
122 C. Lee, E. Z. Xu, Y. Liu, A. Teitelboim, K. Yao, A. Fernandez-Bravo, A. M. Kotulska, S. H. Nam, Y. D. Suh, A. Bednarkiewicz, B. E. Cohen, E. M. Chan and P. J. Schuck, *Nature*, 2021, **589**, 230–235.
123 A. Nexha, J. J. Carvajal, M. C. Pujol, F. Díaz and M. Aguiló, *Nanoscale*, 2021, **13**, 7913–7987.
124 M. Quintanilla and L. M. Liz-Marzán, *Nano Today*, 2018, **19**, 126–145.
125 M. Jia, Z. Fu, G. Liu, Z. Sun, P. Li, A. Zhang, F. Lin, B. Hou and G. Chen, *Adv. Opt. Mater.*, 2020, **8**, 1–7.
126 M. Quintanilla, M. Henriksen-Lacey, C. Renero-Lecuna and L. M. Liz-Marzán, *Chem. Soc. Rev.*, 2022, **51**, 4223–4242.
127 X. Li, Y. Wei, P. Dang, X. Xiao, H. Xiao, G. Zhang, G. Li and J. Lin, *Mater. Res. Bull.*, 2022, **146**, 111592.
128 A. Nexha, M. C. Pujol, J. J. Carvajal, F. Díaz and M. Aguiló, *J. Lumin.*, 2022, **247**, 118854.
129 M. Weber, *Phys. Rev.*, 1968, **171**, 283–291.

130 A. Toncelli, J. Xu, A. Tredicucci, A. M. Heuer and C. Kränkel, *Opt. Mater. Express*, 2019, **9**, 4464.
131 L. E. Muresan, E.-J. Popovici, E. Bica, A. I. Cadis, I. Perhaita and L. B. Tudoran, *J. Therm. Anal. Calorim.*, 2012, **110**, 341–348.
132 K. Elzbieciak, A. Bednarkiewicz and L. Marciniak, *Sens. Actuators, B*, 2018, **269**, 96–102.
133 A. Tymiński, T. Grzyb and S. Lis, *J. Am. Ceram. Soc.*, 2016, **99**, 3300–3308.
134 H. Suo, X. Zhao, Z. Zhang, Y. Wu and C. Guo, *ACS Appl. Mater. Interfaces*, 2018, **10**, 39912–39920.
135 F. H. L. Starsich, P. Gschwend, A. Sergeyev, R. Grange and S. E. Pratsinis, *Chem. Mater.*, 2017, **29**, 8158–8166.
136 A. R. Khadiev, S. L. Korableva, A. K. Ginkel, O. A. Morozov, A. S. Nizamutdinov, V. V. Semashko and M. S. Pudovkin, *Opt. Mater.*, 2022, **134**, 1–9.
137 J. F. Suyver, J. Grimm, M. K. van Veen, D. Biner, K. W. Krämer and H. U. Güdel, *J. Lumin.*, 2006, **117**, 1–12.
138 C. Renero-Lecuna, R. Martín-Rodríguez, R. Valiente, J. González, F. Rodríguez, K. W. Krämer and H. U. Güdel, *Chem. Mater.*, 2011, **23**, 3442–3448.
139 A. Drozdowski, N. Jurga, D. Przybylska, J. C. Brandmeier, Z. Farka, H. H. Gorris and T. Grzyb, *J. Colloid Interface Sci.*, 2023, **649**, 49–57.
140 N. Jurga, D. Przybylska, P. Kamiński, A. Tymiński, B. F. Grześkowiak and T. Grzyb, *J. Colloid Interface Sci.*, 2022, **606**, 1421–1434.
141 M. V. DaCosta, S. Doughan, Y. Han and U. J. Krull, *Anal. Chim. Acta*, 2014, **832**, 1–33.
142 V. Muhr, S. Wilhelm, T. Hirsch and O. S. Wolfbeis, *Acc. Chem. Res.*, 2014, **47**, 3481–3493.
143 L. Xu, J. Li, K. Lu, S. Wen, H. Chen, M. K. Shahzad, E. Zhao, H. Li, J. Ren, J. Zhang and L. Liu, *ACS Appl. Nano Mater.*, 2020, **3**, 2517–2526.
144 N. Jurga, D. Przybylska, P. Kamiński and T. Grzyb, *Sci. Rep.*, 2021, **11**, 18846.
145 M. Runowski, P. Woźny, I. R. Martín, K. Soler-Carracedo, T. Zheng, H. Hemmerich, F. Rivera-López, J. Moszczyński, P. Kulpiński and S. Feldmann, *Adv. Funct. Mater.*, 2024, **34**, 2307791.
146 M. Runowski, D. Marcinkowski, K. Soler-Carracedo, A. Gorczyński, E. Ewert, P. Woźny and I. R. Martín, *ACS Appl. Mater. Interfaces*, 2023, **15**, 3244–3252.